Effect of slip and thermal gradient on micropolar nano suspension flow across a moving hydrogen fuel-cell membrane.

SACHHIN, S.M., MAHABALESHWAR, U.S. and CHAN. A.

2024

International Journal of Hydrogen Energy 63 (2024) 59–81

Contents lists available at ScienceDirect

International Journal of Hydrogen Energy

journal homepage: www.elsevier.com/locate/he

Effect of slip and thermal gradient on micropolar nano suspension flow across a moving hydrogen fuel-cell membrane

S.M. Sachhin [a], U.S. Mahabaleshwar [a], A. Chan [b,*]

[a] Department of Studies in Mathematics, Davangere University, Shivagangothri, Davangere, 577 007, India
[b] School of Engineering, Robert Gordon University, Aberdeen, AB10 7GJ, United Kingdom

ARTICLE INFO

Handling Editor: Dr A Bhatnagar

Keywords:
Radiation
Heat source/sink
Nanoparticle
Micropolar fluid
Mass transpiration

ABSTRACT

The present article examines the micropolar fluid flow with nanofluid suspension across porous stretching/shrinking surfaces with added heat transfer through heat source/sink and radiation. The situation arises in the electrolytic fluid flow across fuel-cell membranes in advanced batteries or fuel cells. To understand the flows and the efficacy of the fuel cell, we study the fluid dynamics of the flow across such shrinking/stretching membranes by converting the non-dimensional governing partial differential equations to ordinary differential equations by using suitable similarity transforms. The energy equation is then analytically solved using hypergeometric series. It is noted that there is a lack of study on nanofluids in the circumstances of micropolar and radiation with porous media. The novelty of the present problem is to examine the influence of micropolar nanofluid flow with heat transfer over permeable surfaces. Analyses show that increasing the rate of shrinking/stretching boundary and increasing the Darcy number decreases the velocity of the fluid while increasing the Eringen number decreases the skin friction decreases dramatically, and increasing the thermal radiation and heat source/sink parameters enhances the thermal boundary layer. Other variations of parameters are also studied and explained graphically. The current work has many useful implications in efficient fuel-cell developments, developing nanofluid has significantly improved the heat transmission process for manufacturing with applications in engineering, biological, and physical sciences.

1. Introduction

Nanofluid plays a major role in industrial applications, especially when suspended with tiny solid particles in a conventional base fluid. It is known to produce good thermal and electrical conductivity which has many important applications in the cooling process and instance fuel cells. Eringen [1,2] is first to introduce the concept of micropolar fluid and give a mathematical model for the behaviour of fluids which provides certain microscopic effects rising from the local structure and micro motions of the fluid elements such as liquid crystals, polymeric fluids, and animal blood. Mahin et al. [3] documents recent developments in nanofluid flow modeling and simulation. Anusha et al. [4] studies the magnetic flow of hybrid nanofluids through a porous stretched surface involving mass flow and the Brinkman model. Kim et al. [5] focuses on the effects of nanofluids and nanostructured surfaces on critical heat flux (CHF) rise while Khan et al. [6] studies the nanofluids flow across stretched surfaces. Mahabaleshwar et al. [7] investigates the nanofluid flow with a viscosity ratio near an accelerating surface.

The permeable expansion sheet induces a far field suction forward a surface and a shrinking surface causes momentum to move away from the surface. Wang et al. [8] conducts research on stagnation flow over shrinking sheets while Waini et al. [9] studies the hybrid nanofluids (HNF) flow, heat transfer with unsteady velocity across stretched sheets. Dash et al. [10] explores the analytical method of stagnation point boundary layer flow over shrunk sheets. Mahabaleshwar et al. [11] studies the influence of radiation and slip on Walter liquid flow across stretched sheets.

Radiation is electromagnetic radiation produced by the thermal motion of particles in matter, and this has attracted quite a bit of attention from many researchers like Sachhin et al. [12] who studies the influence of radiation on ternary nanofluids over porous and mass transpiration across the stretched sheet. Shahsafi et al. [13] conducts research on temperature-normal thermal radiation while Khan et al. [14] focuses on thermal transfer and slip flow on a nanoparticle, dual solutions on the shrunk sheet. Nadeem et al. [15] explores the influence of thermal radiation on Jeffery fluid on a stretched surface. Kenno et al.

* Corresponding author.
E-mail addresses: sachinsm030@gmail.com (S.M. Sachhin), u.s.m@davangereuniversity.ac.in (U.S. Mahabaleshwar), a.chan5@rgu.ac.uk (A. Chan).

https://doi.org/10.1016/j.ijhydene.2024.02.332
Received 15 December 2023; Received in revised form 25 January 2024; Accepted 26 February 2024
Available online 18 March 2024

Nomenclature

Symbols	Description SI unit
A_1, A_2, A_3, A_4	constants **(—)**
a	acceleration $(m\,s^{-1})$
B	temperature slip (K)
C_p	Specific heat capacity $(J\,K^{-1}\,kg^{-1})$
Da	Darcy number (m^{-2})
d	Stretching/shrinking parameter **(—)**
Er	Eringen number **(—)**
f	Velocity stream function $(m^2\,s^{-1})$
g	Gravitational acceleration $(m\,s^{-2})$
h	Rotation **(—)**
j	Inertia per unit mass **(—)**
k_1	Porous media permeability (m^2)
l	Slip parameter $(m\,s^{-1})$
n	Particle concentration $(g\,m^{-3})$
N	Micro rotation component (s^{-1})
N_1	Heat source/sink factor (J)
N_r	Radiation factor (Bq)
Pr	Prandtl number **(—)**
Q_0	Heat source/sink factor t (J)
q_r	Radiative heat flux $(W\,m^{-2})$
S	Mass suction/injection (kg)
T, θ	Temperature (K)
T_w	Surface temperature (K)
T_∞	Ambient temperature (K)
u, v	(x, y) velocity components $(m\,s^{-1})$
(x, y)	Coordinate (m)
β	Solution domain (m)
η	Similarity variable (kg)
γ	Spin gradient viscosity $(m^2\,s^{-1})$
κ	Thermal conductivity $(W\,m^{-1}\,K^{-1})$
κ^*	Absorption coefficient $(W\,m^{-1}\,K^{-1})$
μ	Dynamic viscosity $(kg\,m^{-1}\,s^{-1})$
ν	Kinematic viscosity $(m^2\,s^{-1})$
ρ	Density $(kg\,m^{-3})$
ψ	Stream function $(S\,m^{-1})$
σ	Surface tension $(W\,m^{-1}\,K^{-1})$
σ^*	Stefan-Boltzmann constant $(W\,m^{-2}\,K^{-4})$

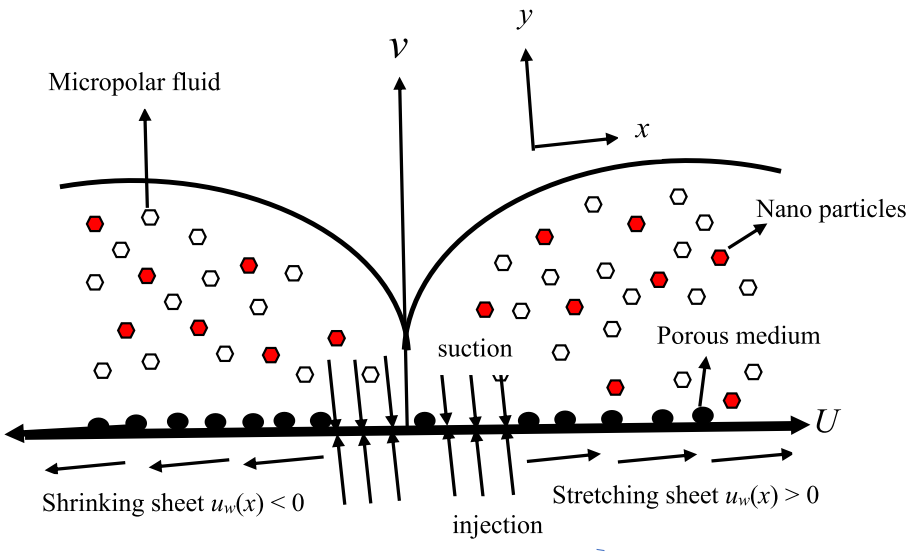

Fig. 1. Schematic diagram of the stretching/shrinking boundary.

[16] focuses on the thermal radiation heat flux of electric thermos influence. Mahabaleshwar et al. [17] explores the magnetohydrodynamic (MHD) effect on HNF flow with thermal radiation across a shrinking surface. Maranna et al. [18] focuses on MHD nanofluid flow with entropy and radiation over the stretched surface. Mohan et al. [19] discovers the influence of radiation on by viscous Bingham fluid on a nonlinear shrinking sheet. Khan et al. [20] focuses on axisymmetric HNF and thermal transfer across permeable shrinking surfaces with heat sources. Priyanka et al. [21] conducts research on radiative HNF with a heat source/sink on a porous medium. Elshehawey et al. [22] discovers the impact of MHD and porous media with radiation over the shrunk boundary. Jalili et al. [23] conducts research on ferrofluid flow on suction/injection over stretched sheets. A number of works [24–44] explores the analytical solutions with an unsteady Brinkman model over the stretched sheet. Water-based nanoparticles are used to study the surface temperature by flowing nanofluid past a photovoltaic thermal system [45–47]. The stability concept of hydrogen production is studied by using the combustion of methanal, methane, and octane and calculated conversion efficiency based on their lower heating values using the porous medium [48–50]. The physical aspects of natural convection magnetohydrodynamic flow of Cu/Ethylene glycol-water nanofluid past a porosity vertical stretching sheet under the impact of thermal radiation is studied by Refs. [51–53].

Usafzai et al. [37] studies the micropolar fluid, and we are concentrating on adding nano-particles into the micropolar fluid and temperature jump with heat and mass transpiration, the goal of this investigation is to see the effect of radiation and heat source/sink on nanofluid water flow over stretching/shrinking sheet embedded in porous medium. In the development of efficient fuel cells, one novel approach is to add nanoparticles into the polar fluid base to increase the electric and thermal conductivity, and hence increase power delivery efficiency. As one understands the flow across the membrane determines

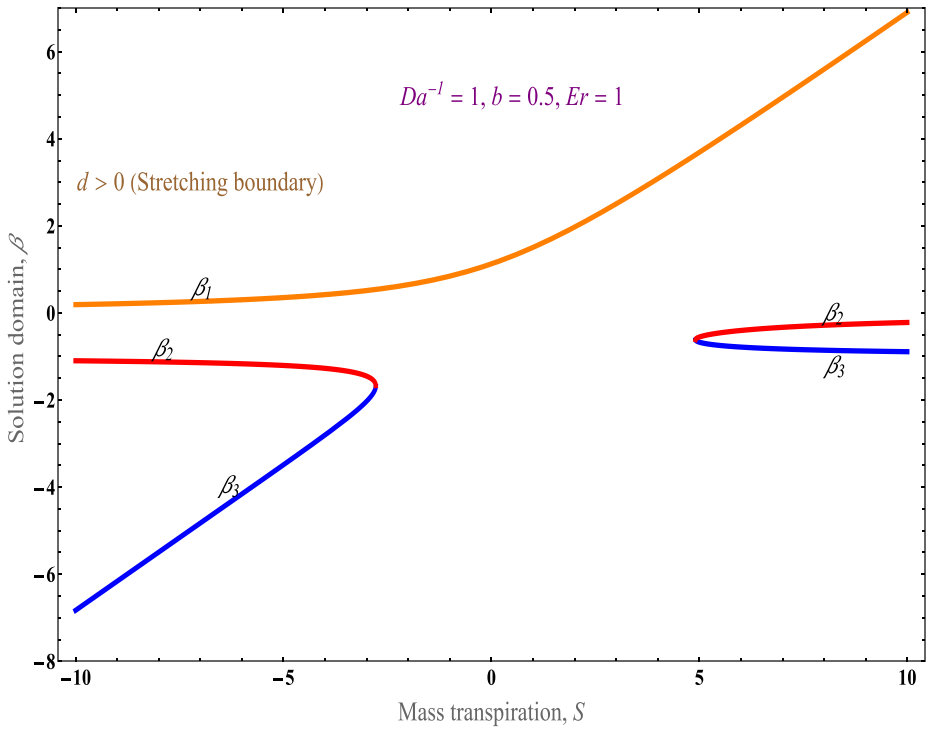

Fig. 2a. Graph of solution domain with mass transpiration on stretching boundary.

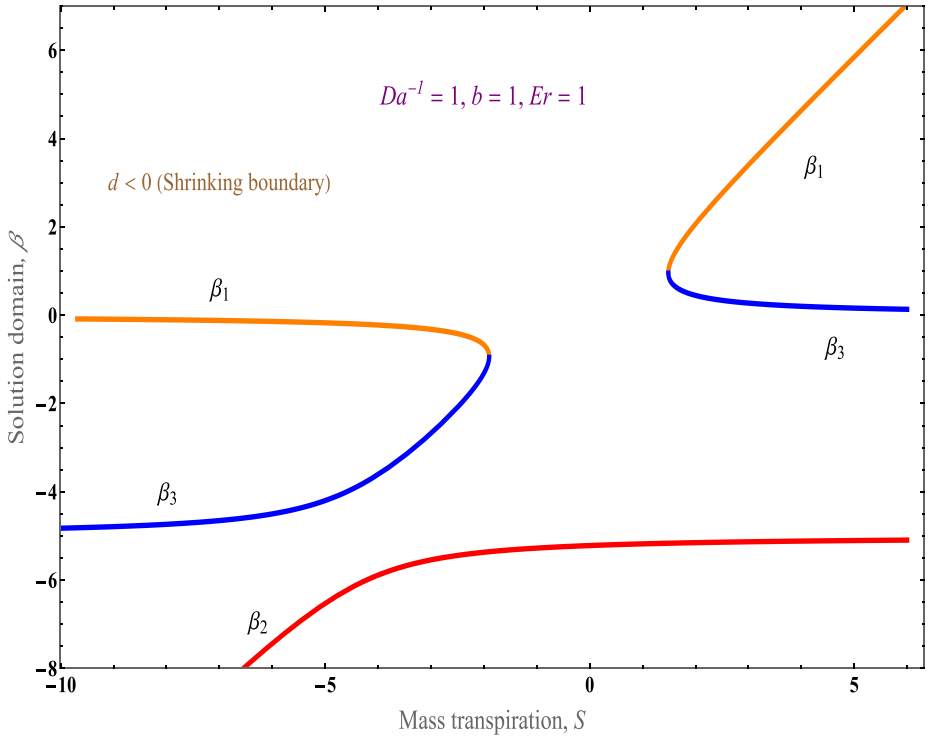

Fig. 2b. Graph of solution domain with mass transpiration on shrinking boundary.

the overall performance of the fuel cell. However, there is a lack of study on micropolar liquids in the circumstances of velocity slip and radiation with permeable media. The current work is to fill this research gap in order to assist the development of fuel cells. The innovation is to combine the velocity slip and temperature jump to the momentum and temperature equations and study the overall flow behaviour of the system. The non-dimensional governing equations are obtained by using suitable similarity transformations and obtaining unique solutions for stretching and shrinking sheets, the results of the current study can be used in other applications like the polymer industry concerning stretching/shrinking sheets. The conductivity and heat transfer rate have a great influence on the performance of the fuel cell and hence proper choice of a fluid and understanding of the fluid flow is very crucial.

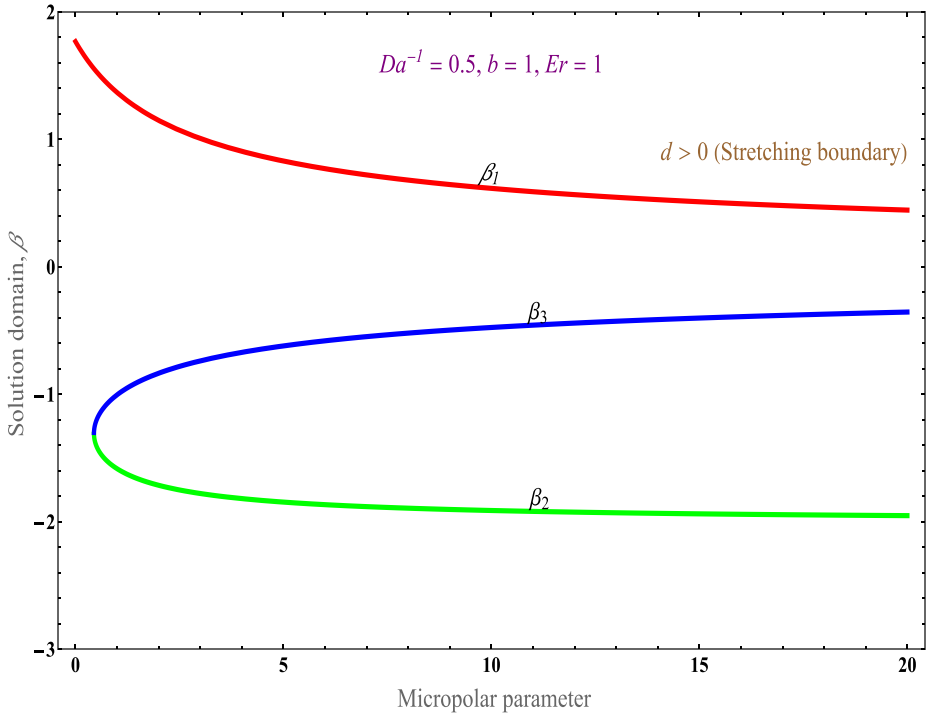

Fig. 3a. Graph of solution domain with micropolar on stretching boundary.

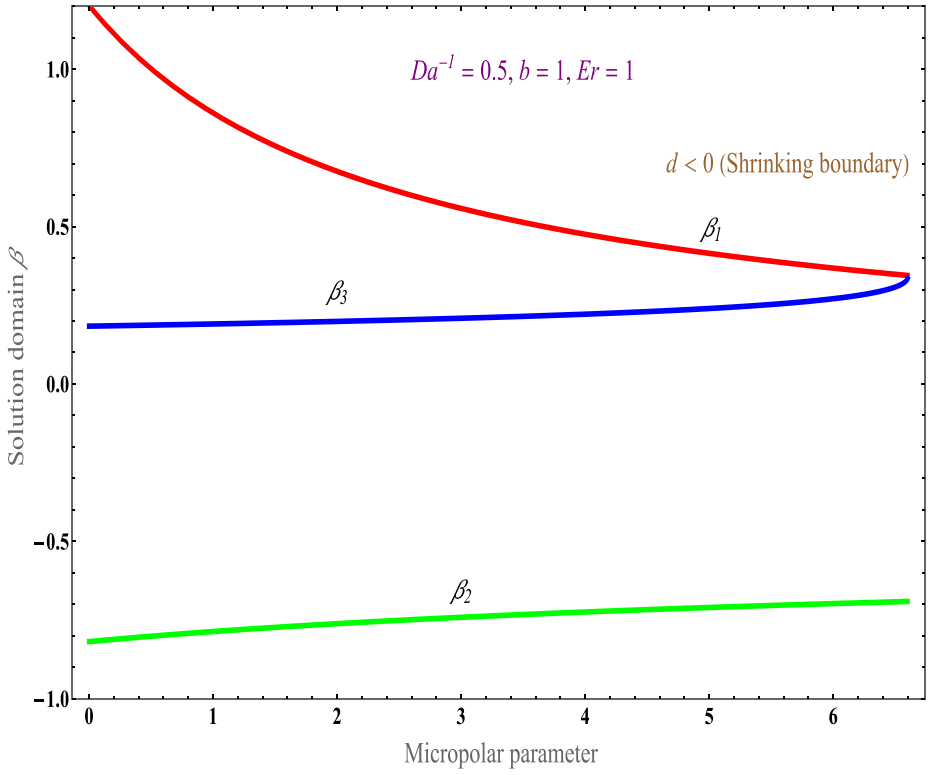

Fig. 3b. Graph of solution domain with micropolar on shrinking boundary.

2. Mathematical formulation and solution

The surface, simulating the flow past the fuel-cell membrane, is placed parallel to the x-axis and perpendicular to the y-axis, and stretches with a velocity $u_w(x) = ax$, where a is a constant. The surface is permeable allowing mass transfer with momentum $v = v_w(x)$, the temperature of the fluid is growing linearly with respect to x, i.e. $T_w(x) = T_w + xT_0$, where T_w is denoted as surface temperature, T_0 is a reference temperature.

The governing equations of the current study micropolar fluid with radiation and heat source/sink with porous media over a stretching/shrinking surface involve the two-dimensional Navier-Stokes equations

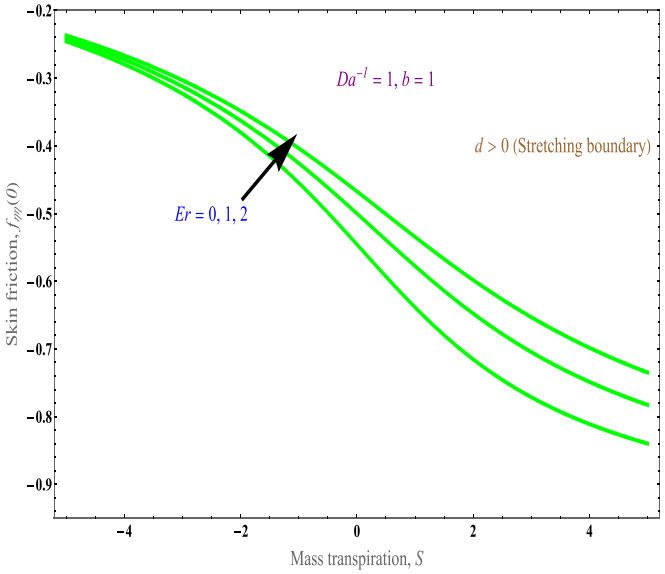

Fig. 4. Graph of reduced skin friction variation against mass transpiration for different Eringen number.

[31,37], with all nomenclatures given in the earlier section.

Continuity equation, $$\frac{\partial u}{\partial x}+\frac{\partial v}{\partial y}=0, \tag{1}$$

Conservation of momentum, $$u\frac{\partial u}{\partial x}+v\frac{\partial u}{\partial y}=\left(\nu_{nf}+\frac{\kappa_{nf}}{\rho_{nf}}\right)\frac{\partial^2 u}{\partial y^2}+\frac{\kappa_{nf}}{\rho_{nf}}\frac{\partial N}{\partial y}-\frac{\mu_{nf}}{\rho_{nf}k_1}u, \tag{2}$$

Angular momentum, $$u\frac{\partial N}{\partial x}+v\frac{\partial N}{\partial y}=\frac{\gamma^*}{\rho_{nf}}\frac{\partial^2 N}{\partial y^2}-\frac{\kappa_{nf}}{\rho_{nf}j}\left(2N+\frac{\partial u}{\partial y}\right), \tag{3}$$

Temperature equation, $$(\rho C_P)_{nf}\left(u\frac{\partial T}{\partial x}+v\frac{\partial T}{\partial y}\right)=\kappa_{nf}\frac{\partial^2 T}{\partial y^2}+Q_0(T-T_\infty)-\frac{\partial q_r}{\partial y}, \tag{4}$$

with the spin gradient viscosity modelled as

$$\gamma=\left(\mu+\frac{\kappa}{2}\right)j=\mu\left(1+\frac{\mathrm{Er}}{2}\right)j, \tag{5}$$

where j is the Eringen parameter for micropolar fluid concerned with fluids with certain microscopic effects arising from the local structure and the micromotions of fluid elements. N is the angular velocity of the solution, with the aim of this hypothesis to ensure the desired performance of the field equations, even in the restrictive case of negligible microstructure effects and the total spin becoming the angular velocity [36].

Using the above the boundary conditions become [37],

$$\left.\begin{aligned} u &= du_w(x)+l\frac{\partial u}{\partial y},\ v=v_w \\ N &= -n\frac{\partial u}{\partial y} \\ T &= dT_w(x)+\kappa_1\frac{\partial T}{\partial y} \end{aligned}\right\}\text{as } y=0,$$

$$u=0, N=0, T=\infty, \text{as } y=\infty, \tag{6}$$

where l is the velocity slip parameter [37]. It is worth mentioning that fluid flow with slip is important in micro-rotational fluids as the flow in the system deviates significantly from the traditional no-slip flow because of the microscale dimensions. Here v_w is the mass flux, $v_w > 0$ is mass injection, $v_w < 0$ is the mass suction respectively, d is the wall deforming parameter with $d > 0$ denotes stretching, $d < 0$ denotes shrinking sheet, and κ_1 is the temperature jump coefficient, n is the concentration of microparticle ranging $0 \le n \le 1$, the linear relationship between the micromovements N and the wall shear $\frac{\partial u}{\partial y}$ is set for analysing the effect of different surface conditions for micro-movements

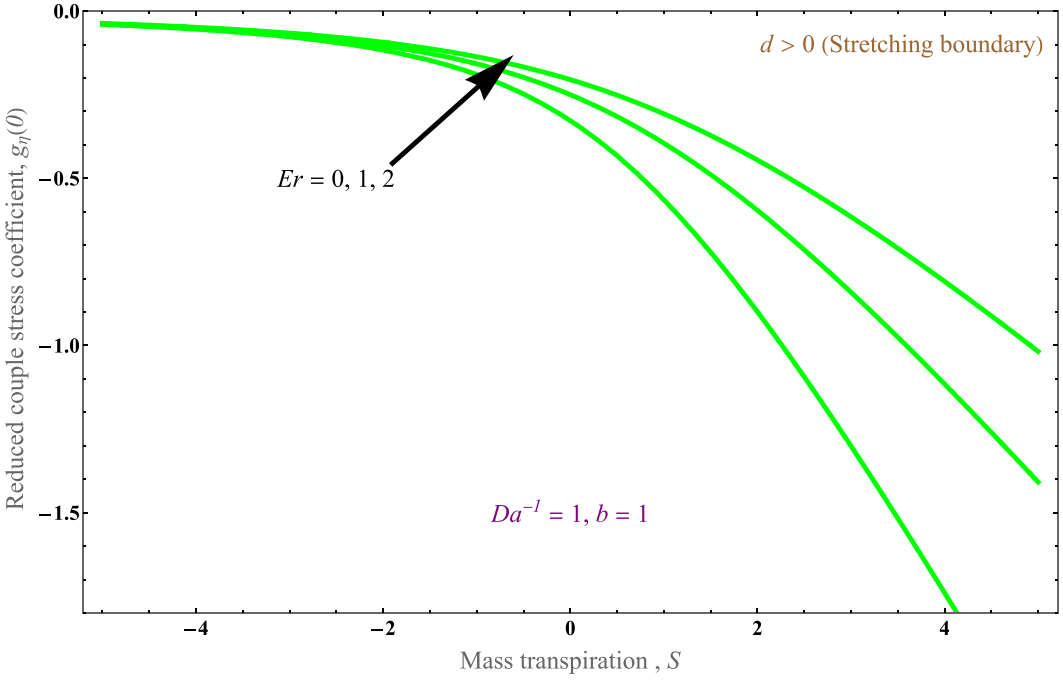

Fig. 5. Graph of reduced coupled stress variation against mass transpiration for different Eringen number.

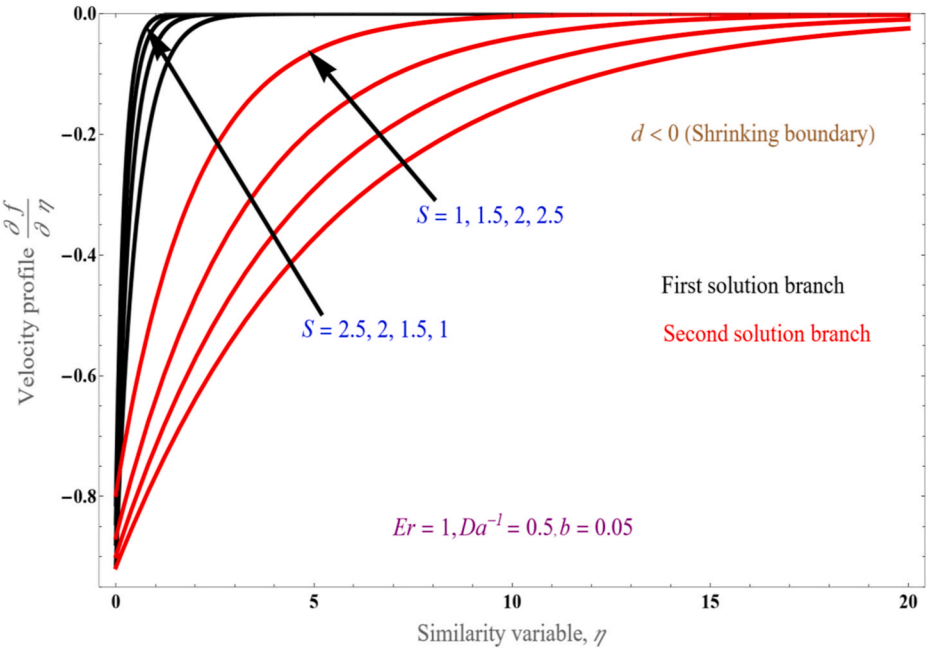

Fig. 6a. Graph of velocity with variation of suction for shrinking boundary.

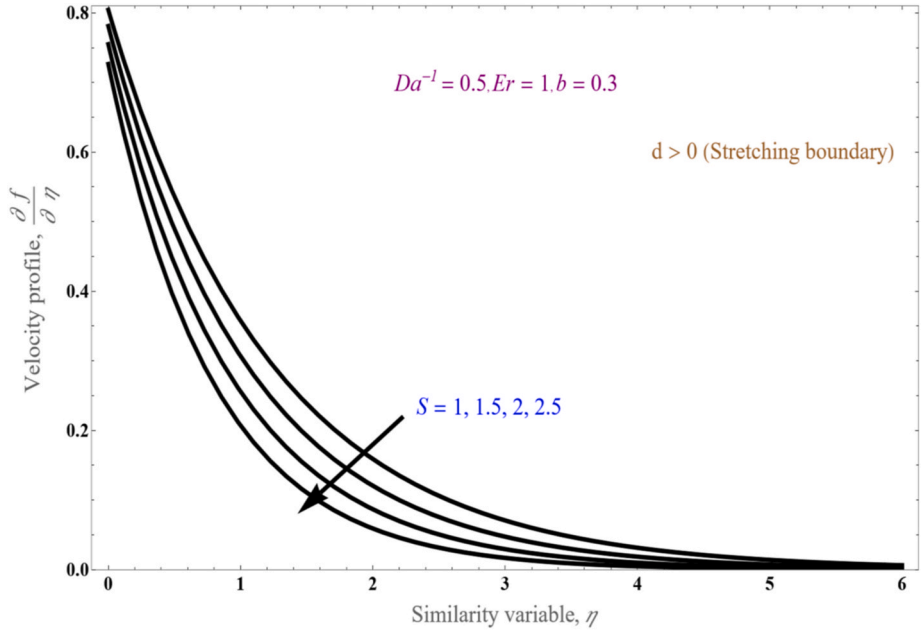

Fig. 6b. Velocity profile with variation of suction for stretching boundary.

The suitable similarity variables are [20,37]:

$$\left.\begin{aligned} \psi &= f(\eta)x\sqrt{a\nu} \\ \eta &= \sqrt{\frac{a}{\nu}}y \\ N &= g(\eta)ax\sqrt{\frac{a}{\nu}} \end{aligned}\right\}, \tag{7}$$

where the stream function is $\psi(x,y)$ defines the velocity as usual by $u = \frac{\partial \psi}{\partial y}$, and $v = -\frac{\partial \psi}{\partial x}$. details the similarity variable. Hence the momentum components become, in terms of similarity variables,

$$\left.\begin{aligned} u &= axf_{\eta}(\eta), v = -\sqrt{a\nu}f(\eta) \\ g(\eta) &= -nf_{\eta\eta}(\eta), \theta(\eta) = \frac{T - T_{\infty}}{T_w - T_{\infty}} \end{aligned}\right\}. \tag{8}$$

Based on Rosseland's approximation, the radiative flux q_r is defined as [14].

$$q_r = -\frac{4\sigma^*}{3k^*}\frac{\partial T^4}{\partial y}, \tag{9}$$

with the ambient temperature T approximated as

$$T^4 = -3T_{\infty}{}^4 - 4T_{\infty}{}^3T, \tag{10}$$

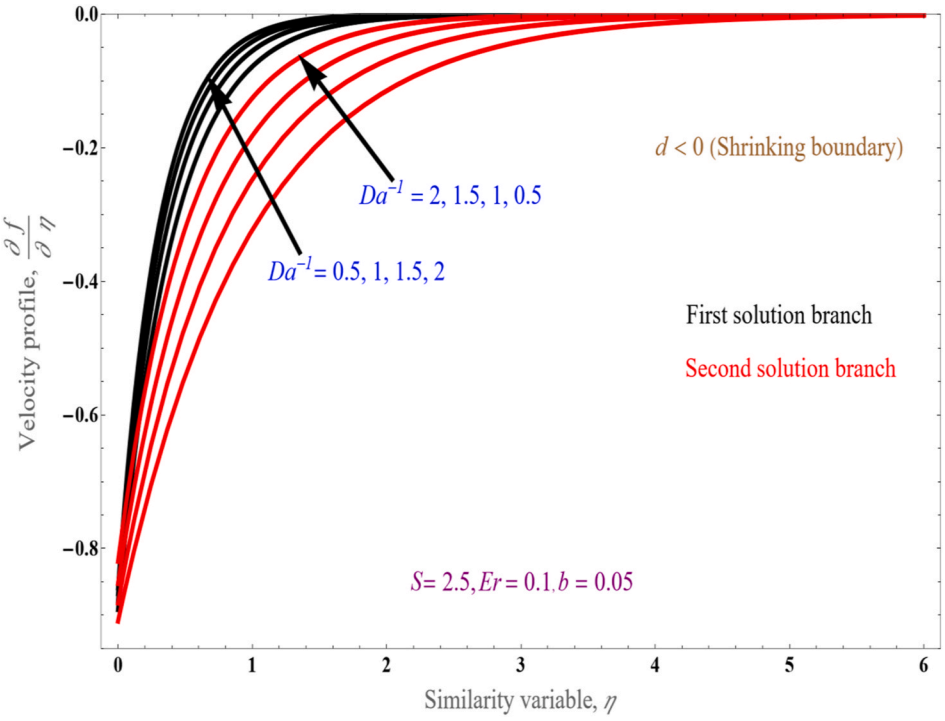

Fig. 7a. Velocity profile with variation of Da^{-1} for shrinking boundary.

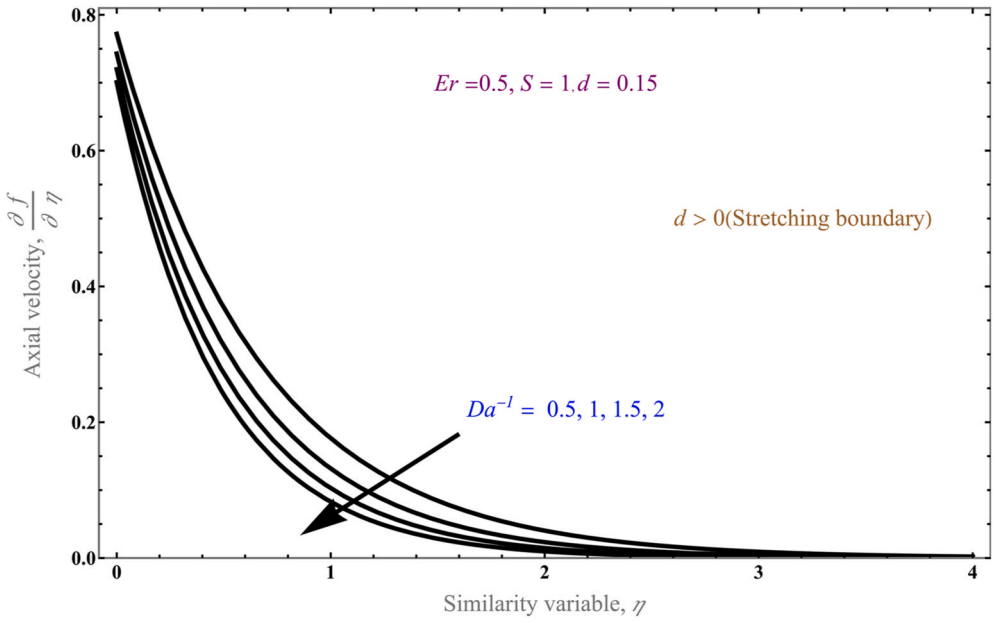

Fig. 7b. Velocity profile with variation of Da^{-1} for stretching boundary.

hence the derivative of heat flux can be obtained by plugging Eq. (10) into Eq. (8) as,

$$\frac{\partial q_r}{\partial y} = -\frac{16\sigma^* T_\infty^3}{3k^*}\frac{\partial^2 T}{\partial y^2}, \tag{11}$$

and combining Eqs. (11) and (4) we obtain,

$$\left(u\frac{\partial T}{\partial x}+v\frac{\partial T}{\partial y}\right) = \left(\frac{\kappa_{nf}}{(\rho C_P)_{nf}}+\frac{1}{(\rho C_P)_{nf}}\frac{16\sigma^* T_\infty^3}{3K*}\right)\frac{\partial^2 T}{\partial y^2}+Q_0(T-T_\infty). \tag{12}$$

Using similarity transformations equations (2)–(4) can be simplified as,

$$(A_1+\mathrm{Er})f_{\eta\eta\eta}(\eta)+A_2\{f(\eta)f_{\eta\eta}-f_\eta(\eta)^2\}-A_1\frac{f_\eta(\eta)}{\mathrm{Da}}+\mathrm{Er}g_\eta(\eta)=0, \tag{13}$$

$$\left(A_1+\frac{\mathrm{Er}}{2}\right)g_{\eta\eta}(\eta)+A_2\{f(\eta)g_\eta(\eta)-f_\eta(\eta)g(\eta)\}-2\mathrm{Er}g(\eta)-\mathrm{Er}f_{\eta\eta}(\eta)=0, \tag{14}$$

$$(A_3+N_r)\theta_{\eta\eta}(\eta)+A_4\,\mathrm{Pr}\{f(\eta)\theta_\eta(\eta)\}+N_i\,\mathrm{Pr}\,\theta(\eta)=0, \tag{15}$$

where

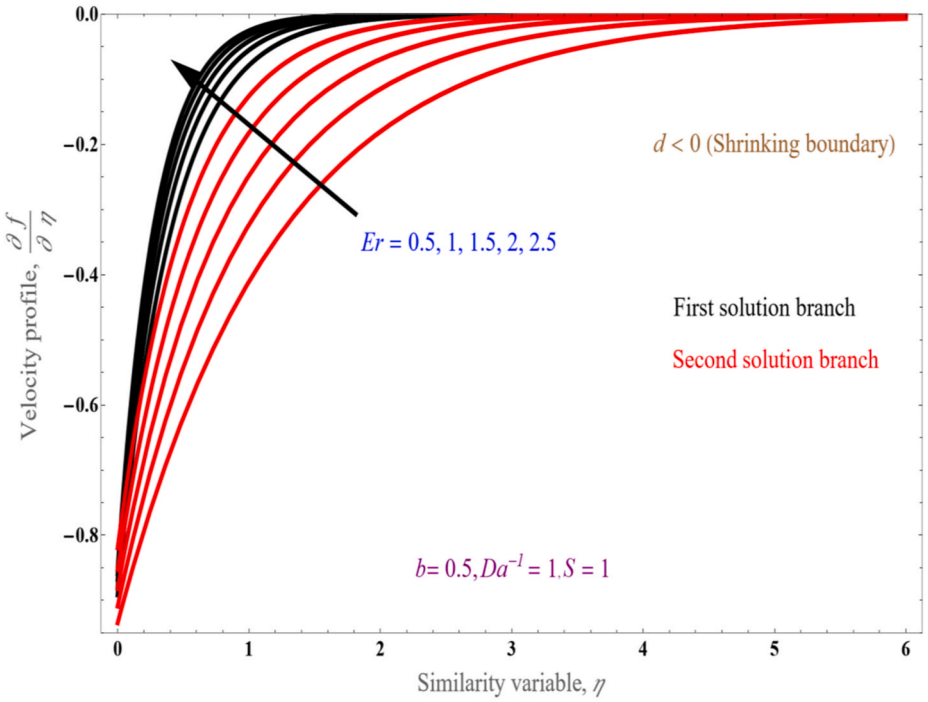

Fig. 8a. Velocity profile for different Eringen number for shrinking boundary.

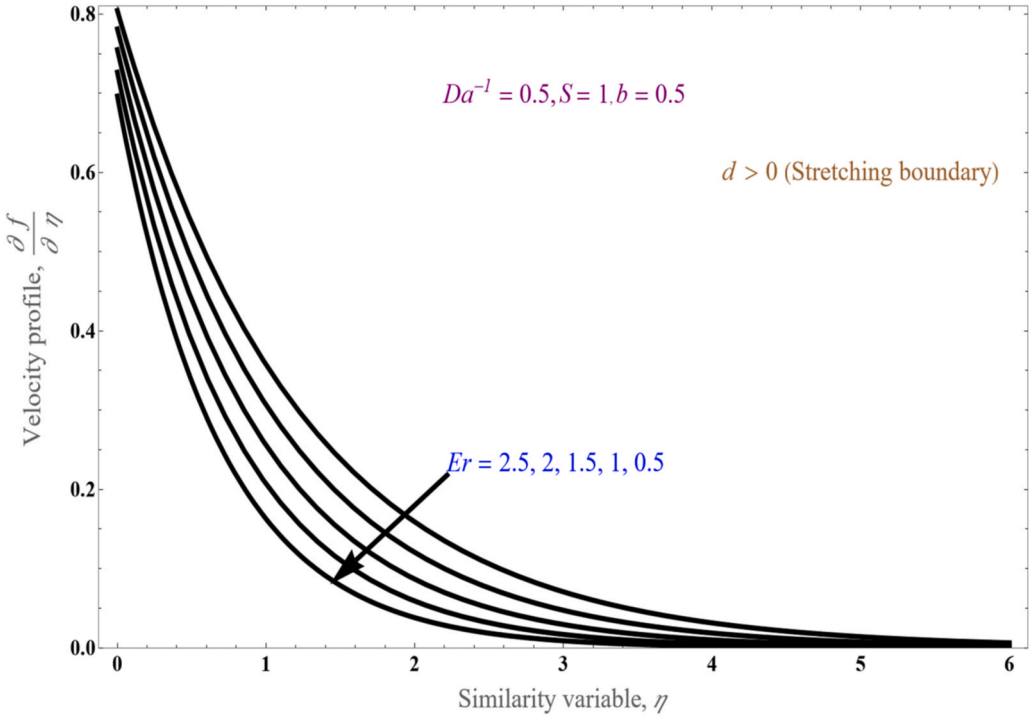

Fig. 8b. Velocity profile for different Eringen number for stretching boundary.

Da $= \frac{ka}{\nu_f}$ is the Darcy number,
Er $= \frac{\kappa}{\mu}$ is the Eringen number,
$N_r = \frac{16\sigma^* T_\infty^3}{3k^* \kappa_f}$ is the radiation term,
Pr $= \frac{\nu_f}{\alpha_f}$ is the Prandtl number,
$N_i = \frac{Q_0}{a(\rho Cp)_f}$ is the heat source/sink,

$$A_1 = \frac{\mu_{nf}}{\mu_f}, A_2 = \frac{\rho_{nf}}{\rho_f}, A_3 = \frac{\kappa_{nf}}{\kappa_f}, A_4 = \frac{(\rho Cp)_{nf}}{(\rho Cp)_f},$$

The boundary conditions are modified as [20,37].

$$\left.\begin{array}{c} f(\eta) = S, f_\eta(\eta) = d + b f_{\eta\eta}(\eta), \\ g(\eta) = -n f_{\eta\eta}(\eta), \theta(\eta) = 1 + B\theta_\eta(\eta), \end{array}\right\} \text{as } \eta \to 0, \tag{16a}$$

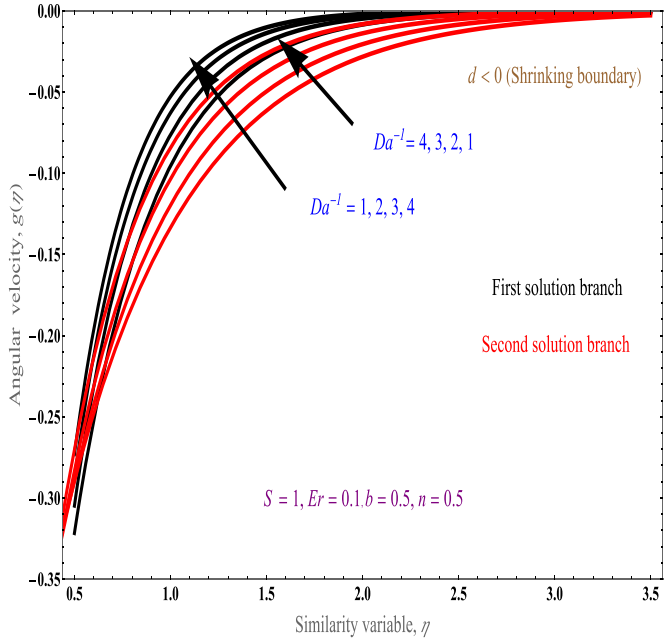

Fig. 9a. Angular velocity profile for different Da^{-1} for shrinking boundary.

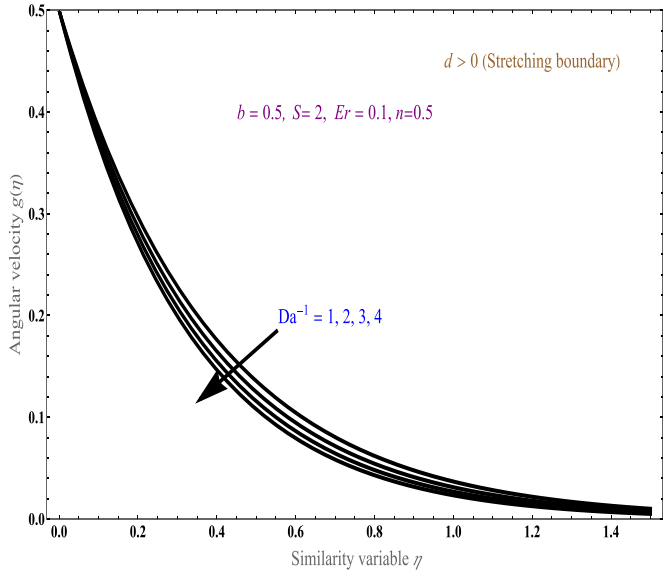

Fig. 9b. Angular velocity profile for different Darcy number for stretching boundary.

$$\lim_{\eta\to\infty} f_\eta(\eta)=0,\ \lim_{\eta\to\infty} g(\eta)=0,\ \lim_{\eta\to\infty}\theta(\eta)=0 \text{ as } \eta>0. \tag{16b}$$

3. Analytical solution for momentum

Solving equations (13) and (14) under modified boundary conditions (16), we obtain the exact solution as below [37],

$$\left.\begin{aligned} f(\eta) &= S + d\frac{1-e^{-\beta\eta}}{(\beta+b\beta^2)},\\ g(\eta) &= \frac{n\alpha\beta}{1+b\beta}e^{-\beta\eta}, \end{aligned}\right\}\ \beta>0, \tag{17}$$

The reducible skin frictions are followed by differentiating equation (17) as,

$$f_\eta(\eta)=\frac{de^{-\beta\eta}}{(1+d\beta)}, g_\eta(\eta)=\frac{-\beta^2 n\alpha e^{-\beta\eta}}{(1+d\beta)}, \tag{18a}$$

$$f_{\eta\eta}(\eta)=\frac{-\beta de^{-\beta\eta}}{(1+d\beta)}, g_{\eta\eta}(\eta)=\frac{\beta^3 n\alpha e^{-\beta\eta}}{(1+d\beta)}, \tag{18b}$$

$$f_{\eta\eta}(0)=\frac{-\beta d}{(1+d\beta)}, g_{\eta\eta}(0)=\frac{\beta^3 n\alpha}{(1+d\beta)}. \tag{18c}$$

where β is to be determined, differentiate the above equations, substitute in equations (13) and (14), and put $n=\frac{1}{2}$ taking as weak concentration case shows the anti-symmetric part of the stress tensor consequently vanishes [37]. This suggests that in a fine particle suspension the particle rotation equals the surface velocity. For $n=0$ means no spin condition as prescribed by Jena and Mathur [38]. The case $n=1$ it represents the turbulent boundary layer flows [39], leading to the following cubic equation,

$$(2A_1b+\mathrm{Er}b)\beta^3+(2A_1+\mathrm{Er}-2A_2Sb)\beta^2-\left(2A_2S+\frac{2A_1b}{\mathrm{Da}}\right)\beta - \left(2A_2d+\frac{2A_1}{\mathrm{Da}}\right)=0, \tag{19}$$

which can be simplified as

$$\xi_1\beta^3+\xi_2\beta^2+\xi_3\beta+\xi_4=0, \tag{20a}$$

where $\xi_1=2A_1b+\mathrm{Er}b, \xi_2=2A_1+\mathrm{Er}-2A_2Sb,$

$$\xi_3=-2A_2S-\frac{2A_1b}{\mathrm{Da}}, \xi_4=-2A_2d-2\frac{2A_1}{\mathrm{Da}}. \tag{20b}$$

All three possible roots of equation (20) can be solved as

$$\beta_1=\frac{-\frac{\xi_2}{3\xi_1}-\left(2^{\frac{1}{3}}\left(-\xi_2^2+3\xi_1\xi_3\right)\right)}{3\xi_1\left(z+\sqrt{4\left(-\xi_2^2+3\xi_1\xi_3\right)^3+(z)^2}\right)^{\frac{1}{3}}} + \frac{1}{32^{\frac{1}{3}}\xi_1}\left(z+\sqrt{4\left(-\xi_2^2+3\xi_1\xi_3\right)^3+(z)^2}\right)^{\frac{1}{3}}, \tag{21a}$$

$$\beta_2=\frac{-\frac{\xi_2}{3\xi_1}+\left(\left(1+i\sqrt{3}\right)\left(-\xi_2^2+3\xi_1\xi_3\right)\right)}{3\xi_1 2^{\frac{1}{3}}\left(z+\sqrt{4\left(-\xi_2^2+3\xi_1\xi_3\right)^3+(a)^2}\right)^{\frac{1}{3}}} - \frac{1+i\sqrt{3}}{6\xi_1 2^{\frac{1}{3}}}\left(z+\sqrt{4\left(-\xi_2^2+3\xi_1\xi_3\right)^3+(z)^2}\right)^{\frac{1}{3}}, \tag{21b}$$

$$\beta_3=\frac{-\frac{\xi_2}{3\xi_1}-\left(\left(1+i\sqrt{3}\right)\left(-\xi_2^2+3\xi_1\xi_3\right)\right)}{3\xi_1 2^{\frac{1}{3}}\left(z+\sqrt{4\left(-\xi_2^2+3\xi_1\xi_3\right)^3+(a)^2}\right)^{\frac{1}{3}}} - \frac{1+i\sqrt{3}}{6\xi_1 2^{\frac{1}{3}}}\left(z+\sqrt{4\left(-\xi_2^2+3\xi_1\xi_3\right)^3+(z)^2}\right)^{\frac{1}{3}}, \tag{21c}$$

where

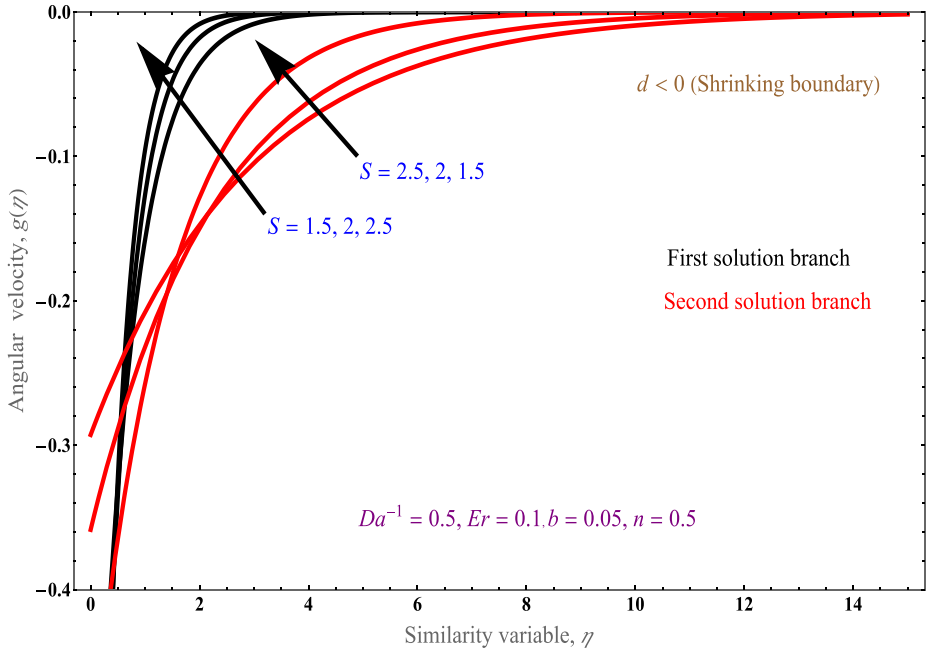

Fig. 10a. Angular velocity profile with different suction for shrinking boundary.

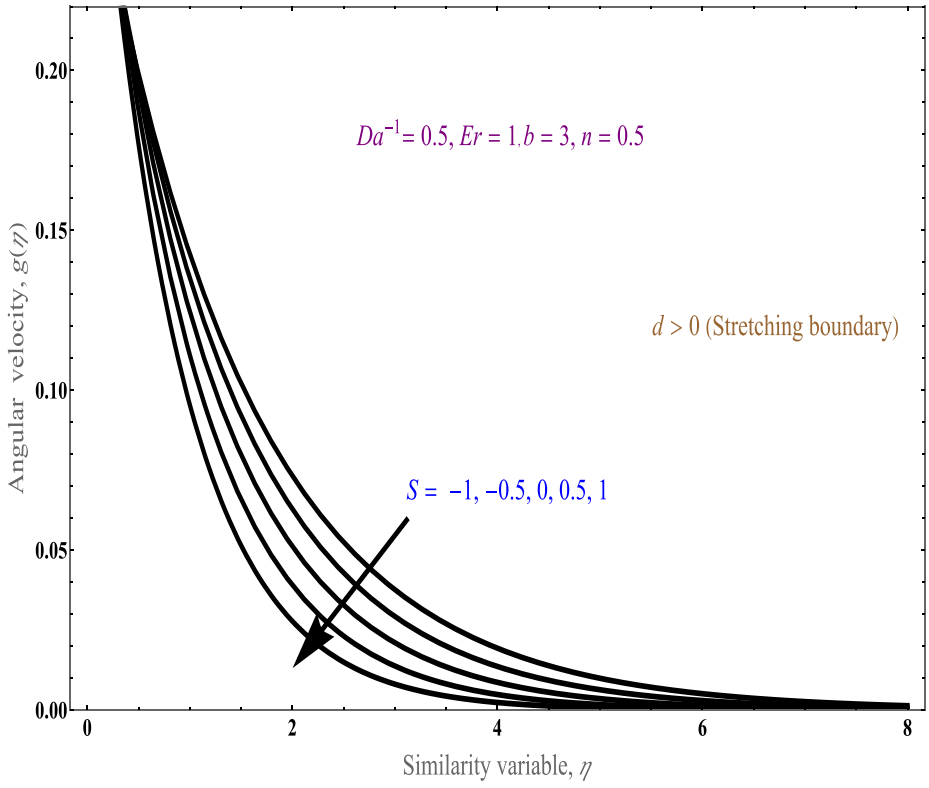

Fig. 10b. Angular velocity profile with different suction for stretching boundary.

$$z = \left(-2\xi_2^3 + 9\xi_1\xi_2\xi_3 - 27\xi_1^2\xi_4\right). \tag{21d}$$

4. Heat transfer analysis

Using all similarity transformation equation (12) convert to the form

$$(A_3 + N_r)\theta_{\eta\eta}(\eta) + A_4\,\mathrm{Pr}\{f(\eta)\theta_\eta(\eta)\} + N_i\,\mathrm{Pr}\,\theta(\eta) = 0, \tag{22}$$

To obtains analytical solution to the above equation, we introduce a new variable $t = e^{-\beta\eta}$, and calculate $\theta, \theta', \theta''$ and then substitute in equation (20a) obtain following equation,

$$t\frac{d^2\theta}{dt^2} + (1 + m + nt)\frac{d\theta}{dt} + L\theta(t), \tag{23a}$$

where

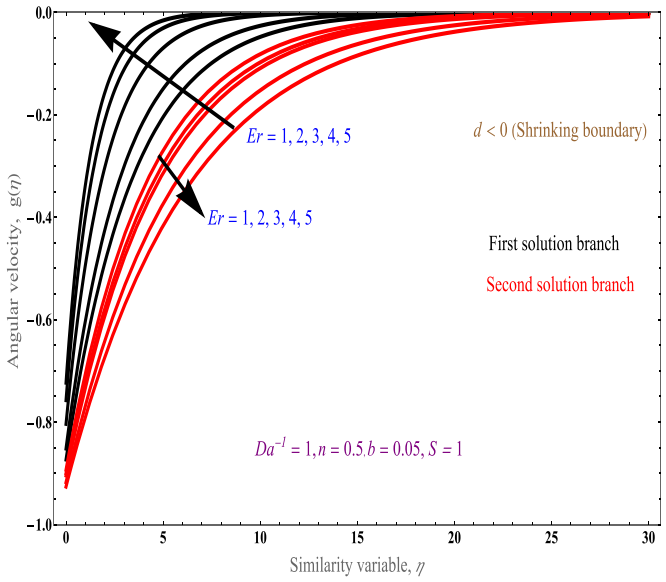

Fig. 11a. Angular velocity profile with different Eringen number for shrinking boundary.

$$n=\frac{A_4\ \mathrm{Pr}\ d}{[A_3+N_r]\beta^2(1+b\beta)}, \tag{23c}$$

$$L=\frac{Q\ \mathrm{Pr}}{[A_3+N_r]\beta^2} \tag{23d}$$

with the boundary constraints

$$\theta(0)=1+B\theta'(0),\theta(\infty)=0. \tag{23e}$$

On applying the Frobenius method, we expand

$$\theta(t)=\sum_{r=0}^{\infty}a_r t^{r+k}, \tag{24}$$

on differentiating above equation to get the following derivatives

$$\theta_\eta(t)=\sum_{r=0}^{\infty}a_r(r+k)\xi^{r+k-1}, \tag{25a}$$

$$\theta_{\eta\eta}(t)=\sum_{r=0}^{\infty}a_r(r+k)(r+k-1)\xi^{r+k-2}. \tag{25b}$$

Applying hypergeometric function $1H_1[a,b,c]$ we obtain

$$\theta(\eta)=a_0\left(e^{-\beta\eta}\right)_1^{-m}H_1\left[(-m+L),1-m,-n\left(e^{-\beta\eta}\right)\right], \tag{26}$$

by applying boundary conditions, we have solutions in terms of Kummer's confluent hypergeometric function as follows,

$$\theta'(0)=\frac{(1-m)_1H_1[(L-m),1-m,-n]}{1H_1[(L-m),1-m,-n]-B\beta(1-m)_1H_1[(L-m),1-m,-n]+B(L-m)n\beta_1H_1[(1+L-m),2-m,-n]}, \tag{27a}$$

$$m=\frac{A_3+N_r}{A_4\ \mathrm{Pr}\frac{1}{\beta}\left(S+\frac{d}{\beta(1+b\beta)}\right)}, \tag{23b}$$

where

β is the solution domain, B is temperature jump parameter, with

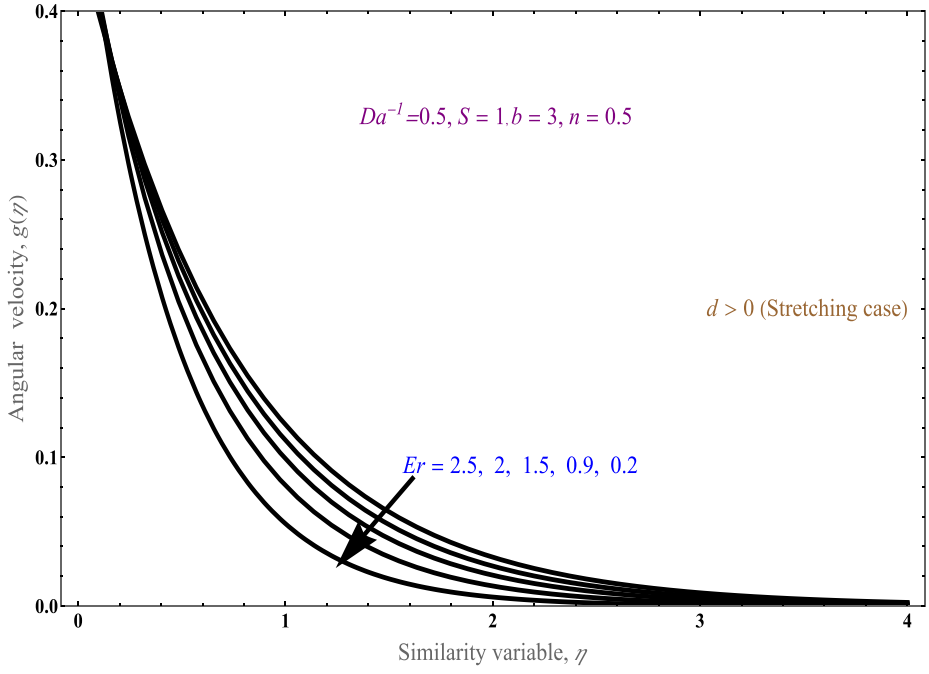

Fig. 11b. Angular velocity profile with different Eringen number for stretching boundary.

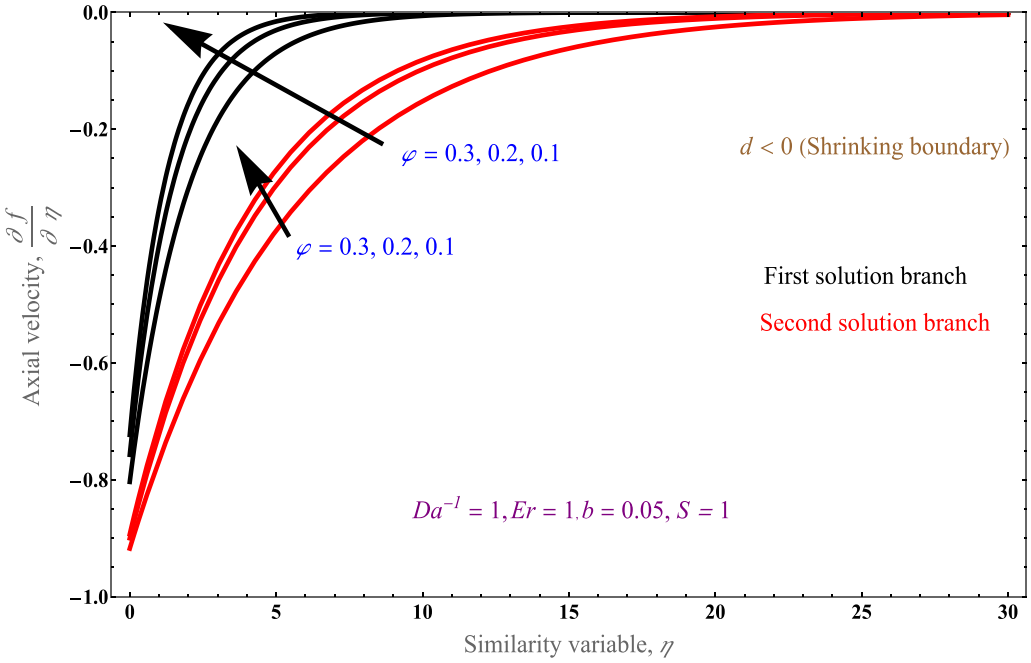

Fig. 12a. Normal velocity profile with various volume fraction for a shrinking boundary.

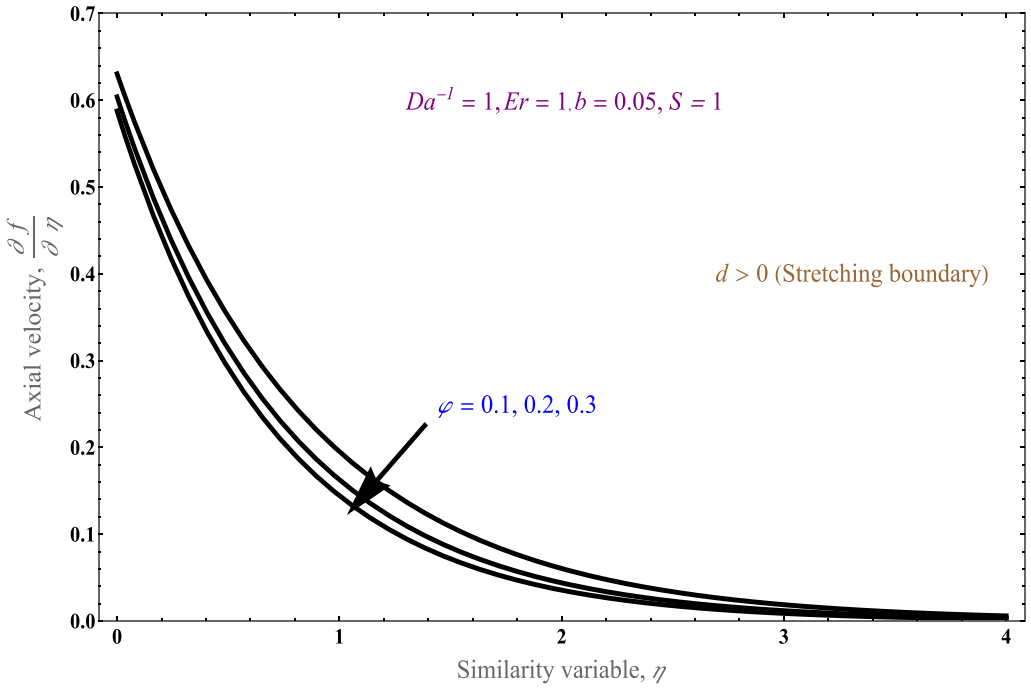

Fig. 12b. Normal velocity profile with various volume fraction for a stretching boundary.

$$m = \frac{A_3 + N_r}{A_4 \Pr \frac{1}{\beta}\left(S + \frac{d}{\beta(1+b\beta)}\right)}, \tag{27b}$$

$$n = \frac{A_4 \Pr d}{(A_3 + N_r)\beta^2(1+b\beta)}, \tag{27c}$$

$$L = \frac{Q \Pr}{(A_3 + N_r)\beta^2}. \tag{27d}$$

5. Results and discussion

The present work concentrates on the study of micropolar fluid with suspension of nanofluid over a porous stretching/shrinking sheet, and investigate the heat transfer process and its relationship with heat source/sink parameter, thermal radiation parameter, porosity to gain a clear insight on the physics of the problem.

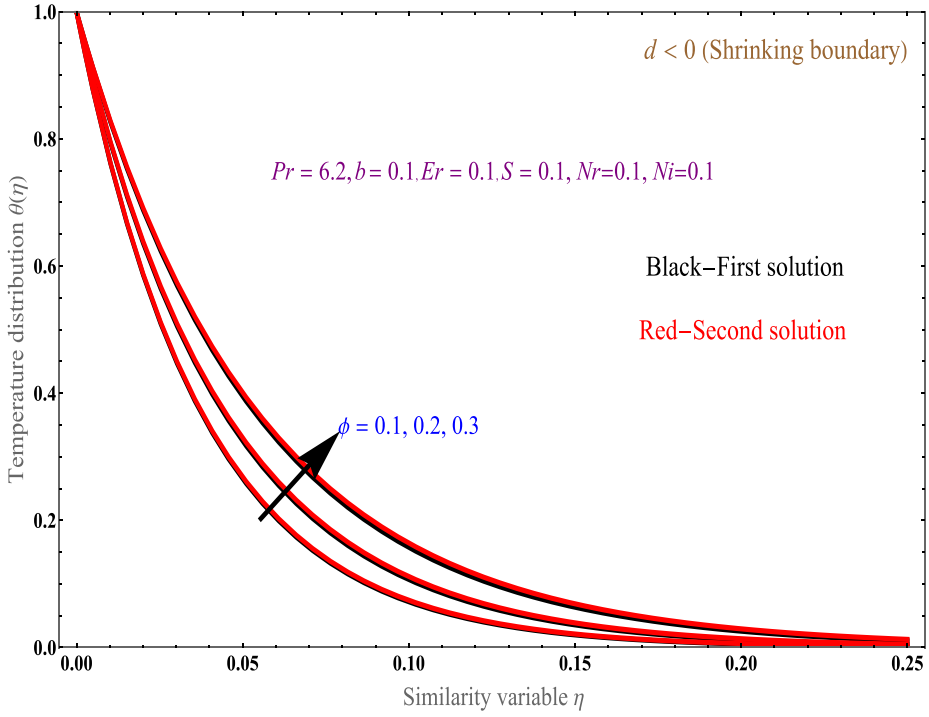

Fig. 12c. Graph of temperature with rising volume fraction.

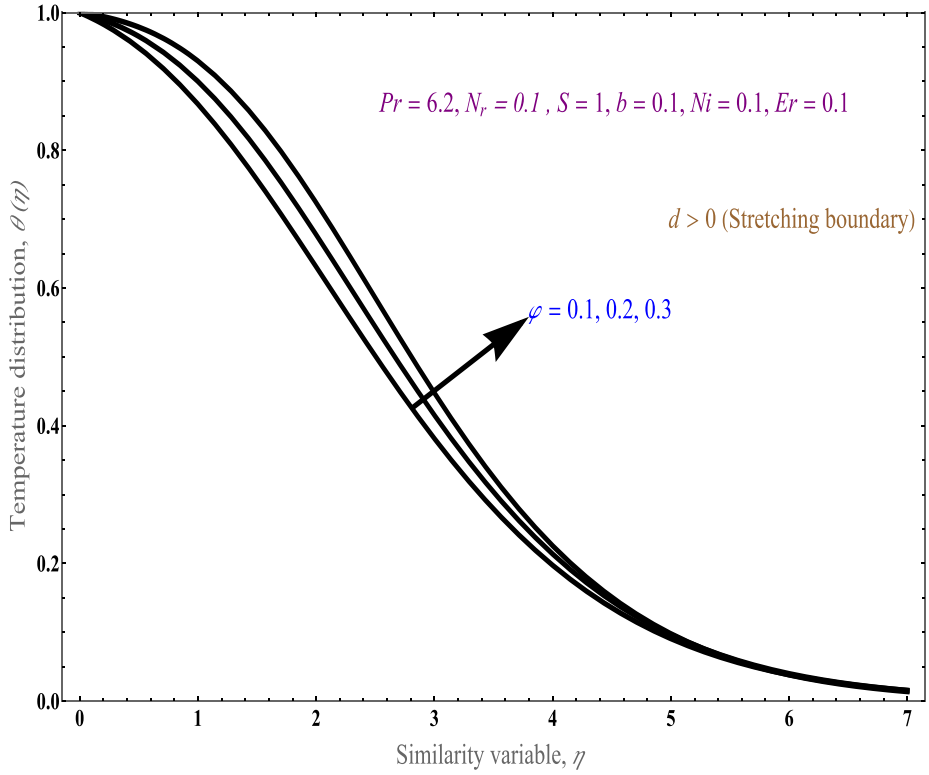

Fig. 12d. Graph of temperature with variation of volume fraction.

5.1. *Thermophysical properties of gold nano particles Table 1 [32]*

The representative values of heat capacity, density, thermal conductivity of nano fluid of gold are used as an example to illustrate the physics of the system [4]. Some properties of the mixture can be determined by the following formulae.

- **Density** $\frac{\rho_{nf}}{\rho_f} = (1-\varphi) + \varphi\left(\frac{\rho_s}{\rho_f}\right)$,
- **Dynamic viscosity** $\frac{\mu_{nf}}{\mu_f} = \frac{1}{(1-\varphi)^{2.5}}$,
- **Heat capacitance** $\frac{(\rho C_p)_{nf}}{(\rho C_p)_f}(1-\varphi) + \varphi\left(\frac{(\rho C_p)_s}{(\rho C_p)_f}\right)$,

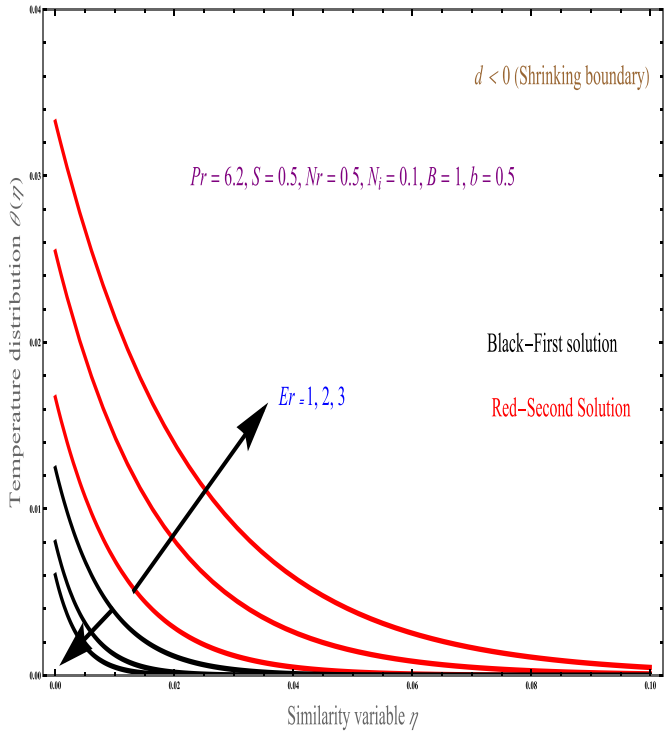

Fig. 13a. Temperature variation for different Eringen micropolar parameter.

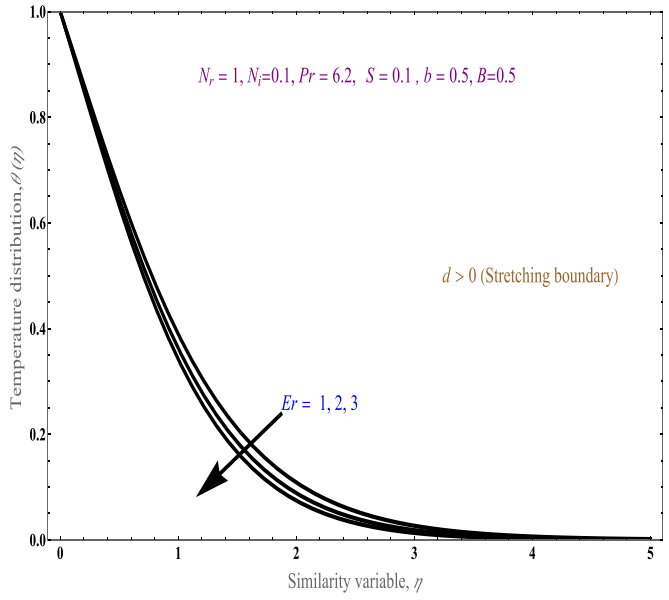

Fig. 13b. Temperature variation for different Eringen number for stretching boundary.

- **Thermal conductivity** $\frac{\kappa_{nf}}{\kappa_f} = \frac{(\kappa_s+2\kappa_f)-2\varphi(\kappa_f-\kappa_s)}{\kappa_s+2\kappa_f+\varphi(\kappa_f-\kappa_s)}$.

Fig. 2(a) and (b) represents the solution domain graphs for stretching/shrinking boundary profile with mass transpiration, while keeping all other parameters constant graphs showing that for shrinking boundary first root solution β_1 shows decreasing nature in the positive region, the third root β_3 shows the increasing nature in the negative region while in the same region the second root solution β_2 shows continuously decreasing nature; in the stretching boundary the first root solution dramatically rises towards the positive region, the second and third root solutions shows decreasing and increasing nature in the negative region (see Fig. 1). In both stretching/shrinking boundary real root solution β_1 exist in the positive region, while other both imaginary β_2, β_3 exist in the negative region,

For a physical system the values of β must be real and hence this graphs define the regions which a physical system can actually exist, depending on which root to follow. It also shows that there are transitions from roots to roots depending parameter changes which at cusp points can lead to critical change in flow behaviours, for instance between β_2 and β_3 in Fig. 2(a) and between β_1 and β_3 in Fig. 2(b). Attentions should be paid to these cusp points to avoid critical changes in flow behaviours.

Similarly, Fig. 3(a) and (b) portray solution domain graphs for stretching/shrinking boundary profile with micropolar parameter, while keeping all other parameters constant, graphs showing that for shrinking boundary the first root solution β_1 shows decreasing nature and third root solution β_3 shows increasing nature, but second root solution β_2 decreases continuously in the negative region, for stretching boundary the first root solution shows continuous increasing nature, second root shows the increasing nature in negative region while in the same region third root β_3 solution shows increasing nature. In both stretching/shrinking boundary only real root solution β_1 lies in the positive region, but in shrinking boundary second solution β_3 also possess in positive region. As in Fig. 2, critical transition takes place between β_2 and β_3 in Fig. 3(a) and between β_1 and β_3 in Fig. 3(b), where attention has to be paid to.

Fig. 4 represents the skin friction graph with mass transpiration for variation of micropolar parameter, while keeping inverse Darcy number and other parameter constant and with positive velocity slip, increasing values of Eringen parameter is connected with stronger rheological effects which tends to decays the velocity gradient. Meanwhile, as the velocity decreases, which reduces energy dissipation and therefore the thermal gradient decreases. The graph shows that the couple stress gradient under increasing values of micropolar parameter is zero on surface and then increases towards the negative direction in stretching boundary. This seems to suggest a way to reduce friction around the membrane, but suitably tuning the suction of the flow around the membrane.

Fig. 5 represents the couple stress graph with mass transpiration for variation of Eringen number, while keeping the inverse Darcy number and other parameter constant and with positive velocity slip. Increasing values of Eringen parameter is connected with stronger rheological effects which tends to decay the velocity gradient. Meanwhile, as the velocity decreases, it similarly decreases the dissipation of energy and therefore the thermal gradient decrease graph shows that while increase the Eringen number the behavior of skin friction decreases dramatically. This again is another measure in which the viscosity of the base fluid can be altered accordingly by altering the suction around the membrane, in order to suit the fuel-cell flow requirements.

Fig. 6(a) and (b) represent the graphs of suction of normal velocity profile with similarity variable, effectively its distance away from the stretching surface, while keeping inverse Darcy number, and other parameters constant. The first graph shows that the shrinking boundary exhibits dual solution: increasing the suction parameter increases the both higher and lower branch solution. In Fig. 6(b) the stretching boundary exhibits the unique solution and while raising the S parameter the solution shows decreasing in nature. The S parameter shows increasing nature for stretching and showing reverse nature for shrinking boundary.

Fig. 7(a) and (b) represent the inverse Darcy number graphs for normal velocity profile against its similarity variable, while keeping Eringen number and other parameters constant, to show how the presence of porous factor will alter the velocity profile and change the fluid flow structure. The flow paths for the flow of the fluid are restricted due to improvement in the shape factor which exhibit frictional and drag force on the liquid. This results in reduction in improvement of velocity

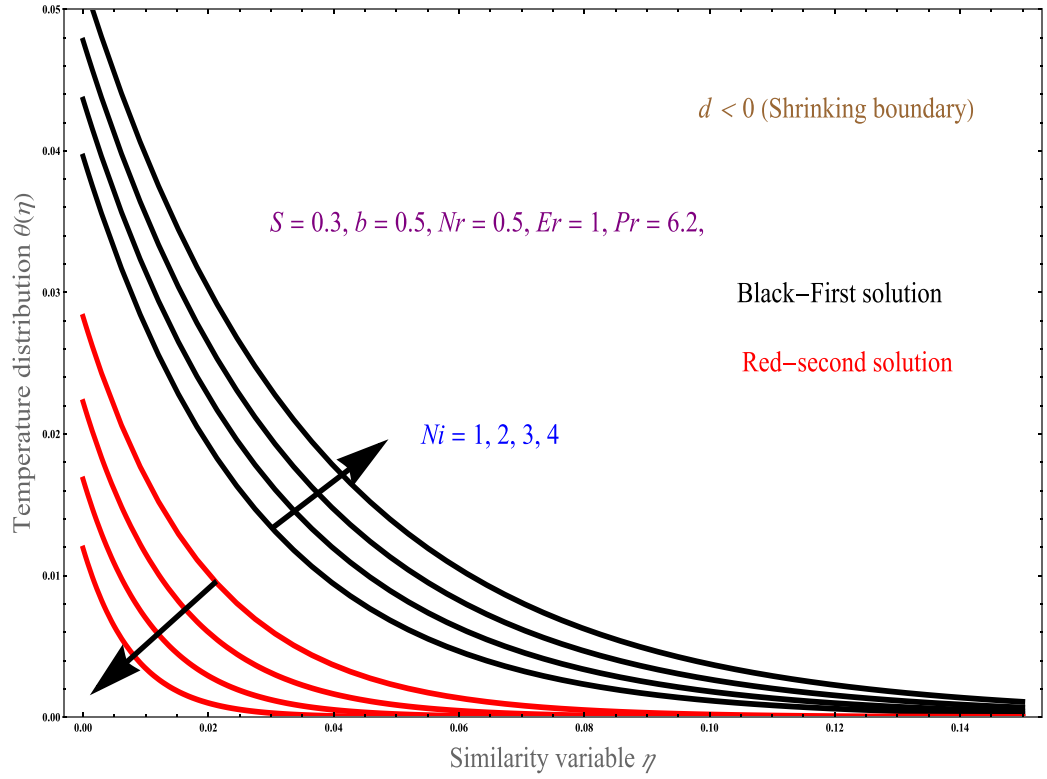

Fig. 14a. Variation of temperature profile for different values N_i. For shrinking boundary.

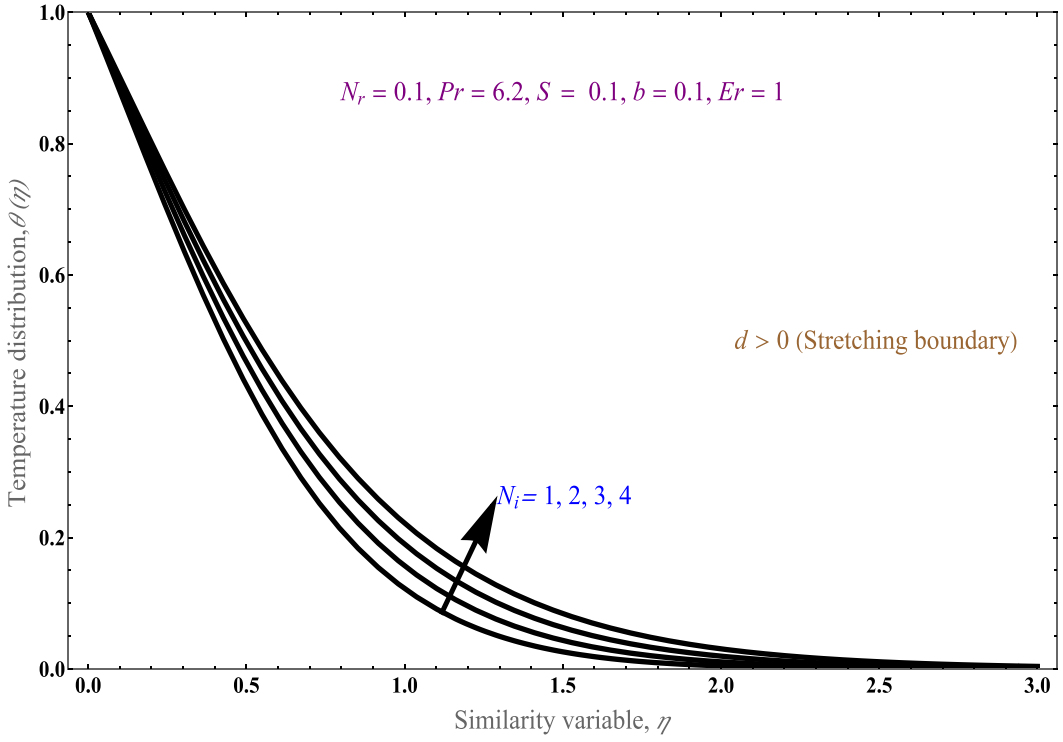

Fig. 14b. Variation of temperature profile for different values N_i. For stretching boundary.

profile. The first graphs shrinking boundary exhibits the dual solution shows the increasing of inverse Darcy parameter increases the both higher and lower branch solution, in the second graph for stretching boundary exhibits the unique solution and while rising the inverse Darcy parameter the solution shows decreasing in nature, inverse Darcy number parameter shows increasing nature for stretching and showing reverse nature for shrinking boundary.

Fig. 8(a) and (b) represent the variation of Eringen number against the normal velocity profile with similarity variable, while keeping inverse Darcy number and other parameters constant. The first graph's

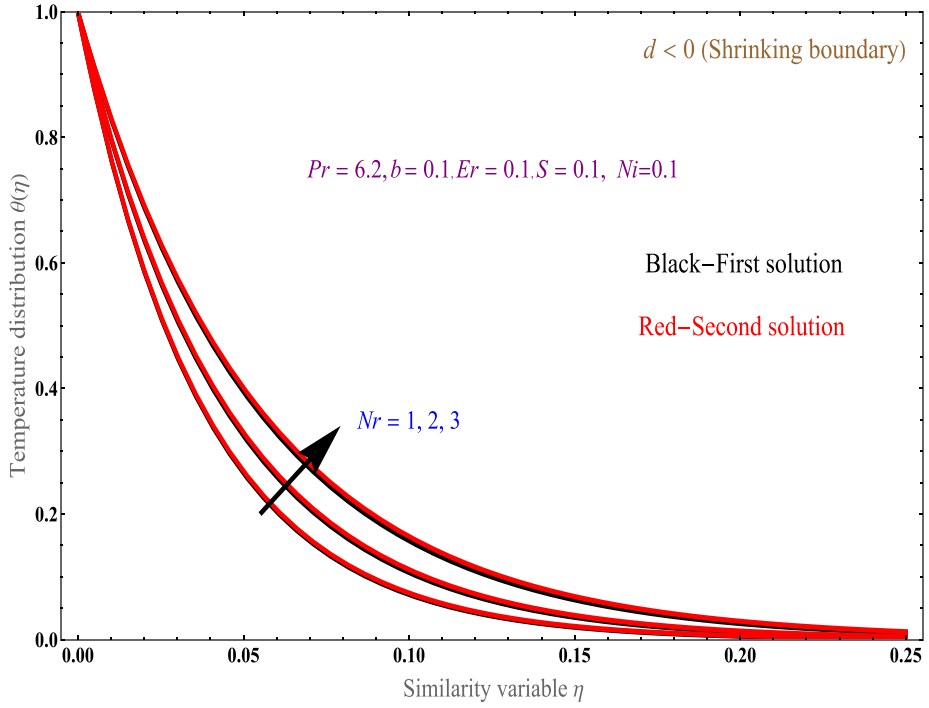

Fig. 15a. Variation of temperature profile for different values of N_r for a shrinking surface.

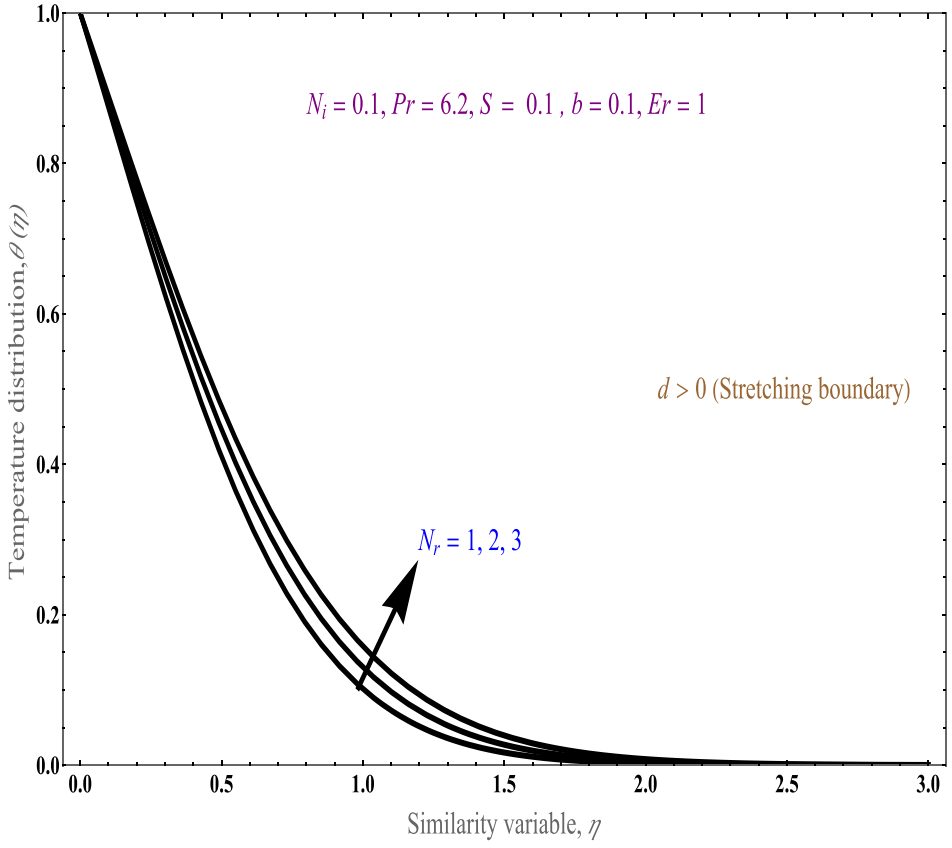

Fig. 15b. Variation of temperature profile for different values of N_r for a stretching surface.

shrinking boundary exhibits dual solution as well: it shows the increasing Eringen number decreases the both higher and lower branch solution. After all the Eringen number is the ratio of thermal conductivity over momentum transfer, and hence increasing Eringen number simply tells that heat transfer is more dominant in the flow. In the second graph for stretching boundary exhibits the unique solution

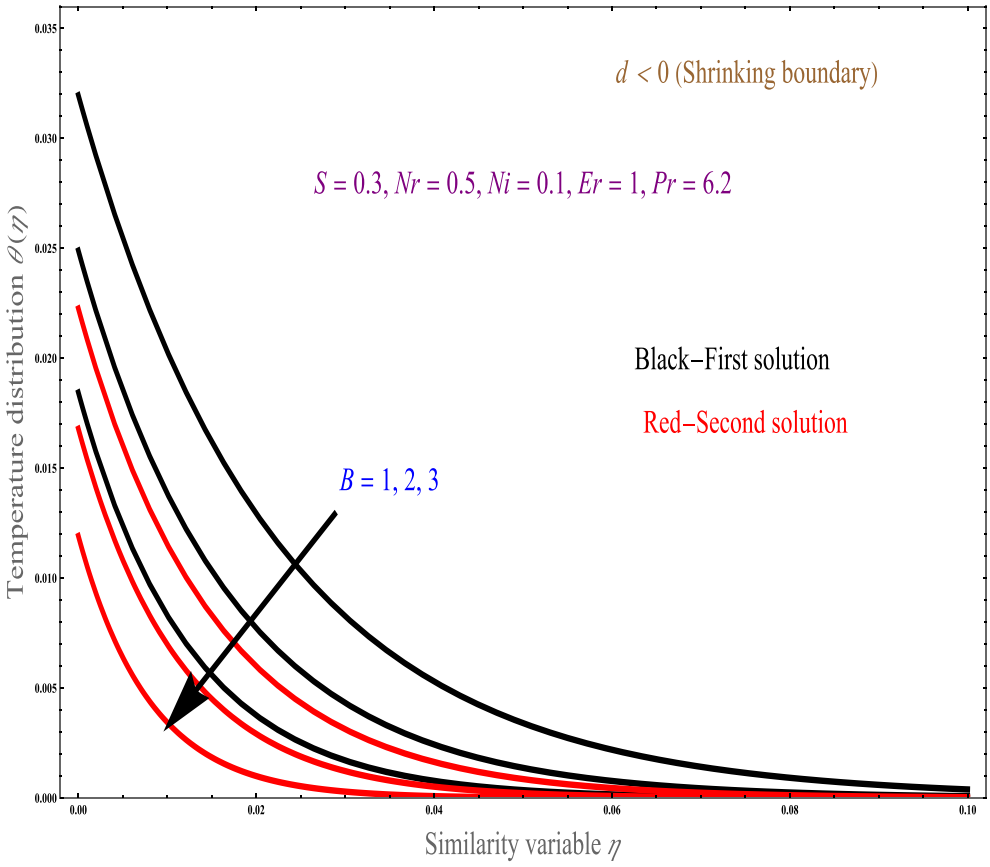

Fig. 16a. Variation of temperature profile for different jump near a shrinking boundary.

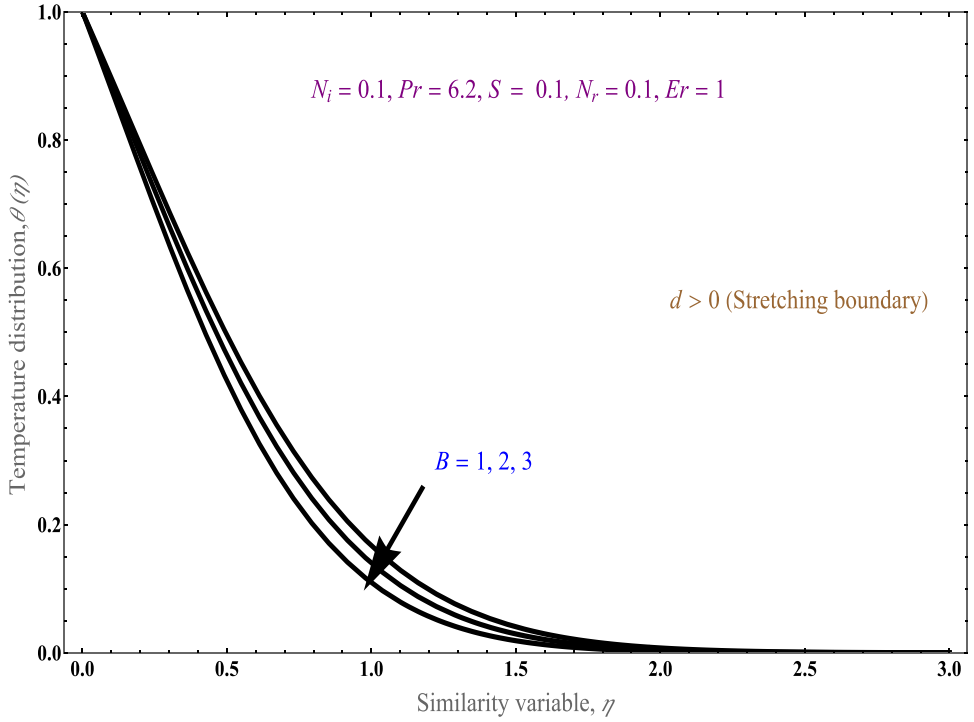

Fig. 16b. Variation of temperature profile for different jump near a stretching boundary.

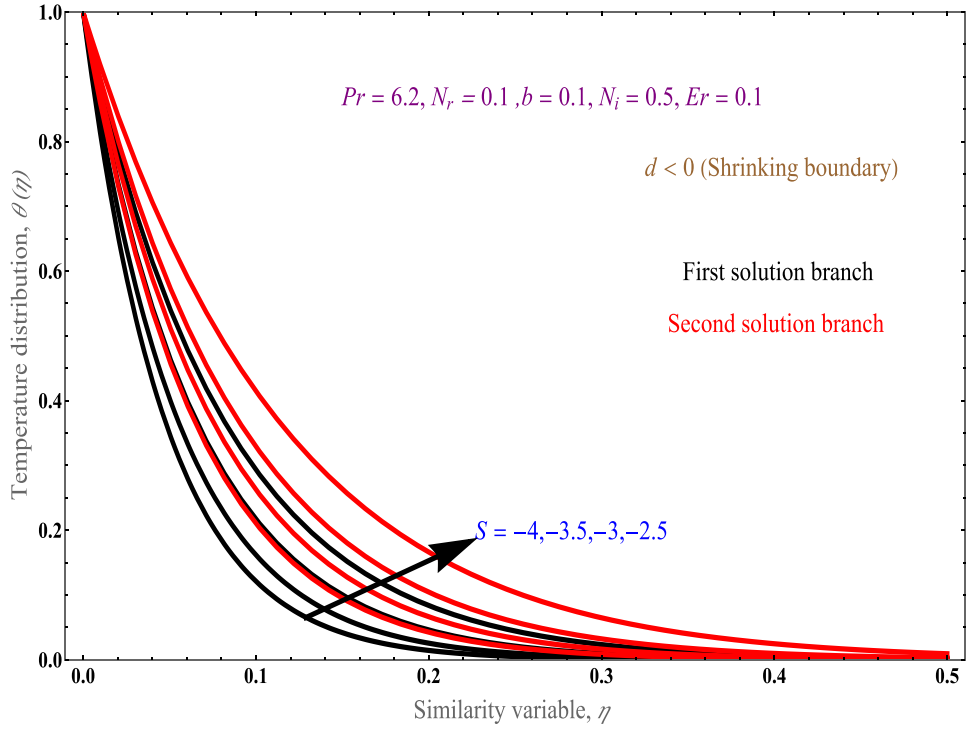

Fig. 17a. Temperature profile for different suction near a shrinking boundary.

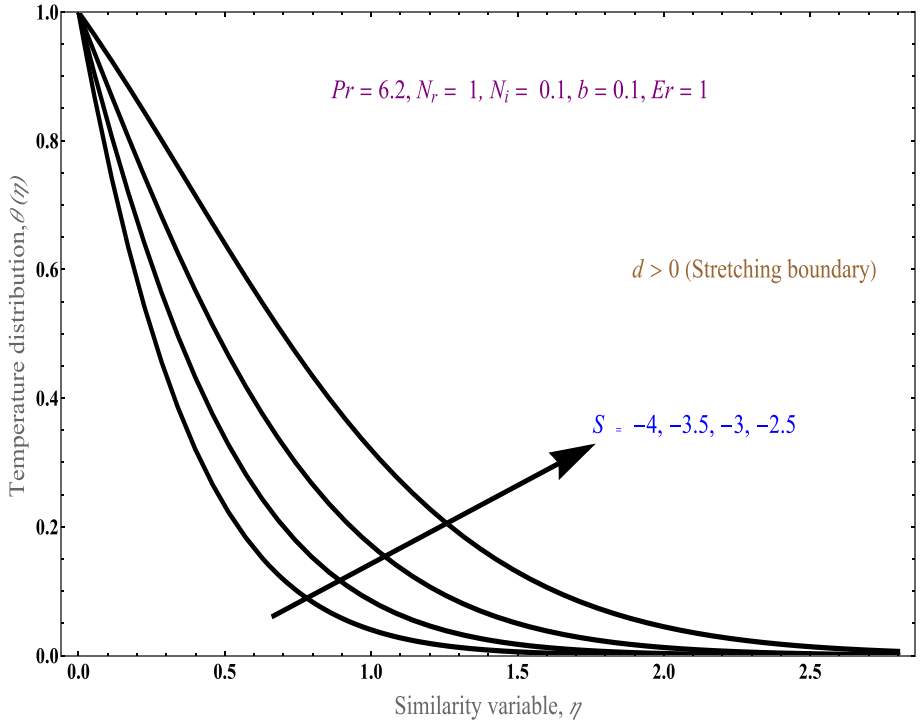

Fig. 17b. Temperature profile for different suction near a stretching boundary.

and while raising Eringen number the solution shows decreasing in nature, Eringen number shows decreasing nature for both stretching/shrinking surface, meaning increase in momentum transfer and hence help electrical conductivity.

Fig. 9(a) and (b) represents the inverse Darcy number graphs for angular velocity profile against distance from the surface, while keeping Eringen number and other parameters constant, and positive velocity slip b. The angular velocity is an indication of the shear flow inside the system. The flow paths for the flow of the fluid are restricted due to improvement in the permeable factor which exhibit frictional and drag force on the liquid. This results in improvement in the thermal profile. the first graphs shrinking boundary exhibits the dual solution shows the increasing of inverse Darcy parameter increases lower branch solution but decays the upper branch solution, in second graph for stretching

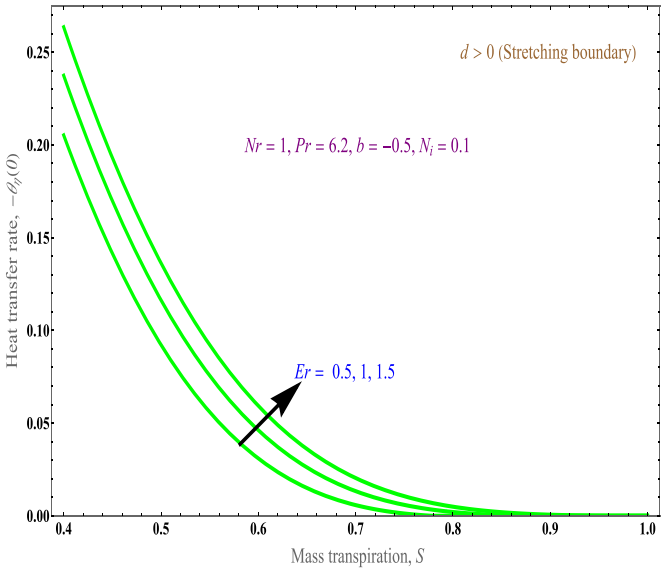

Fig. 18. Variation of heat transfer rate for different Eringen number for stretching boundary.

boundary exhibits the unique solution and while rising the inverse Darcy parameter the solution shows decreasing in nature, inverse Darcy number parameter shows increasing nature for lower branch solution and decreasing nature for upper branch solution for both stretching and shrinking boundary,

Fig. 10(a) and (b) represents the mass transfer graphs for angular velocity profile with similarity variable, with Eringen number, inverse Darcy number constant, and positive velocity slip *b*. The first graph's shrinking boundary exhibits the dual solution shows the increasing of mass transfer parameter increases higher branch solution but decreases lower branch solution. In the second graph for stretching boundary exhibits the unique solution and while rising the mass transfer parameter the solution shows decreasing in nature, mass transfer parameter shows increasing nature for upper branch solution for stretching and decreasing nature for shrinking boundary.

Fig. 11(a) and (b) represents the Eringen number graphs for angular velocity profile with similarity variable, while keeping inverse Darcy number mass transfer parameter constant, with positive slip parameter *b*. Increasing values of Eringen parameter is connected with stronger rheological effects which tends to decay the velocity gradient. Meanwhile, as the velocity declines, the dissipation of energy decreases and therefore the thermal gradient decreases. The first graph shrinking boundary exhibits the dual solution shows the increasing of micropolar parameter decreases the higher branch solution and rises the lower branch solution. In the second graph for stretching boundary exhibits the unique solution and while rising the micropolar parameter the solution shows decreasing in nature, Eringen number shows decreasing nature for shrinking/stretching boundary for first branch solution.

Fig. 12(a) and (b) represents the volume fraction graphs for velocity profile with similarity variable, while keeping inverse Darcy number mass transfer parameter constant, with positive slip parameter *b*. Increasing volume fraction of nanoparticles leads to the enhancement of temperature of central line. The first graph shrinking boundary exhibits the dual solution shows the increasing of volume fraction parameter increasing the both solutions in stretching/shrinking sheet in the fluid region. This points to changing the flow pattern and structure by changing the composition of the fluid itself and hence alter the overall fuel cell performance. The shifting of different branches also causes attention changing the composition may abruptly change the entire flow structure as it reaches critical point.

Fig. 12(c) represents the volume fraction graphs for temperature profile with similarity variable, while keeping radiation, mass transfer, Prandtl number, and other parameters constant. Results indicate that an increase of volume fraction of nanoparticles leads to the enhancement of the volume fraction temperature of central line of flow, rising the volume fraction parameter rises the both upper and lower branch solution for shrinking boundary. Fig. 12(d) represents the volume fraction graphs for temperature profile with similarity variable for stretching boundary,

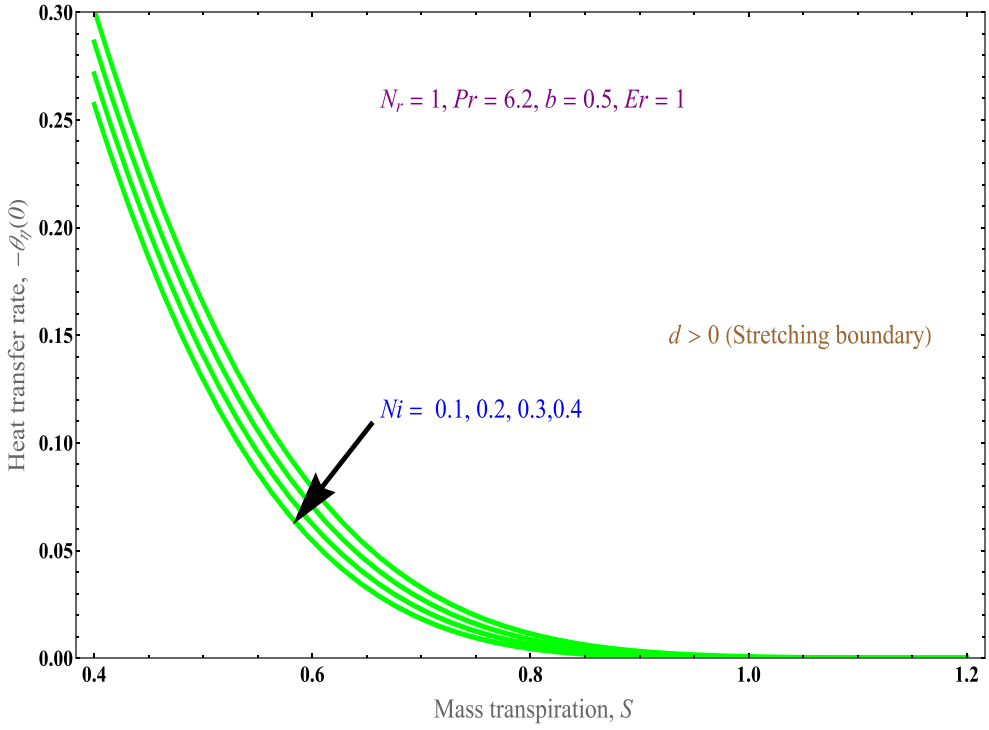

Fig. 19. Variation of heat transfer rate against suction for different mass transfer rate for a stretching boundary.

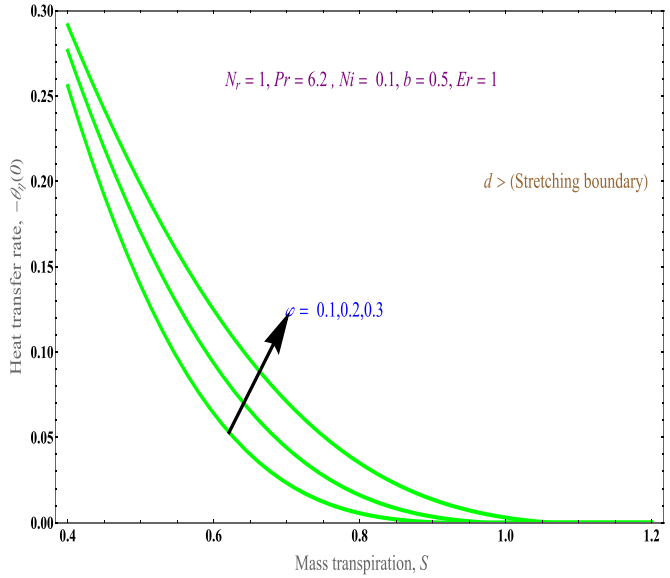

Fig. 20. Variation of heat transfer rate with different volume fraction for a stretching boundary.

while keeping radiation, mass transfer, Prandtl number, and other parameters constant, rising the volume fraction parameter rises the upper branch solution, raising the volume fraction parameter raises both upper and lower branch solution for both stretching/shrinking boundary. An increase in thermal conductivity with the volume fraction nanoparticles, also the thermal boundary layer thickness reduces with an amplify for nanoparticles thus the rate of heat transfer enhances with increases of volume fraction.

Fig. 13(a) and (b) represents the Eringen number graphs for temperature profile with similarity variable, while keeping radiation, heat source/sink, temperature slip, mass transfer parameter constant, with positive slip parameter b. Increasing values of Eringen parameter is connected with stronger rheological effects which tends to decays the velocity gradient, Meanwhile, the velocity is declining, which reasons to decline the dissipation of energy and therefore the thermal gradient decrease, the first graph shrinking boundary exhibits the dual solution shows the increasing of Eringen number decreases the higher branch solution and rising the lower branch solution. In the second graph for stretching boundary exhibits the unique solution and while rising the Eringen number the solution shows decreasing in nature, Eringen number shows decreasing nature for shrinking/stretching boundary for first branch solution,

Fig. 14(a) and (b) represents the heat source/sink graphs for temperature profile with similarity variable, while keeping radiation, Eringen number, temperature slip, mass transfer parameter constant, with positive slip parameter b. The parameter N_i refers to the amount of heat produced/consumed per unit volume. Internal heat generation/absorption actually improves the heat transfer, increase of heat source/sink increases the thickness of thermal boundary layer. Increasing the heat sources intensity corresponds to a greater thermal diffusion layer, presence of heat source limits in the flow state produces more heat, due to the production of energy in the thermal boundary layer. The first graph shrinking boundary exhibits the dual solution shows the increasing of heat source/sink parameter rises higher branch solution and decreases the lower branch solution. In the second graph for stretching boundary exhibits the unique solution and while rising the heat source/sink parameter the solution shows increasing in nature, heat source/sink parameter shows increasing nature for both shrinking/stretching boundary for first branch solution.

Fig. 15(a) and (b) represents the thermal radiation graphs for temperature profile with similarity variable, while keeping heat source/sink, Eringen number, temperature slip, mass transfer parameters constant, with positive slip parameter b. The temperature boundary layer thickness increases in radiation absorption throughout the boundary layer region the temperature of the fluid strengthens with reinforcement in time for both stretching/shrinking case, radiation behaves like a supporting force which accelerates the fluid particles near the vicinity of the plate. It is also noted that temperature boundary layer thickness increases when radiation tends to increase inside a boundary layer region. The first graph shrinking boundary exhibits the dual solution shows the increasing of thermal radiation parameter increases the both higher branch and lower branch solution. In the second graph for stretching boundary exhibits the unique solution and while rising the thermal radiation parameter the solution shows increasing in nature,

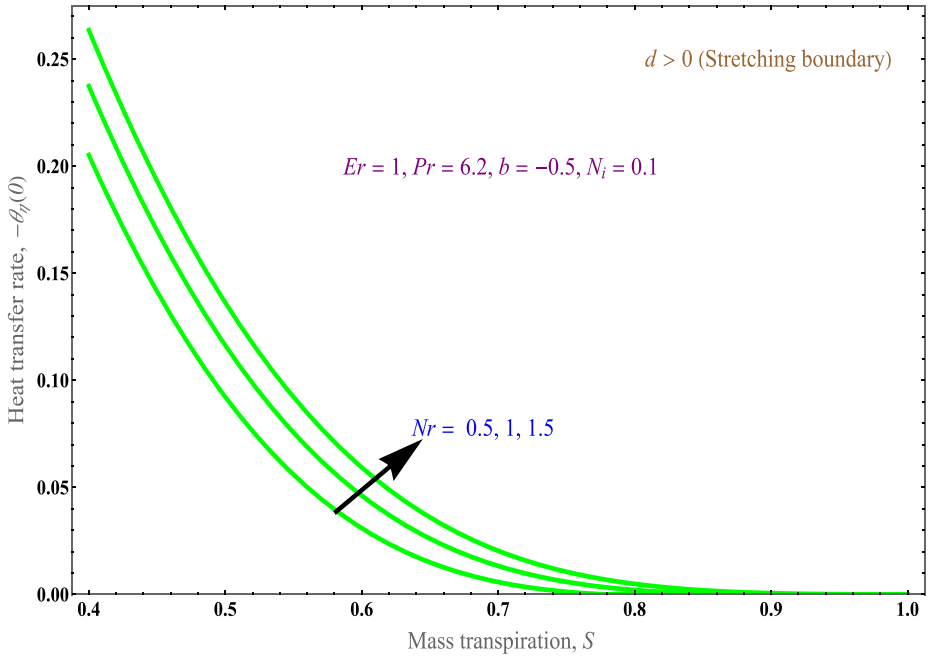

Fig. 21. Variation of heat transfer rate for different of radiation for a stretching boundary.

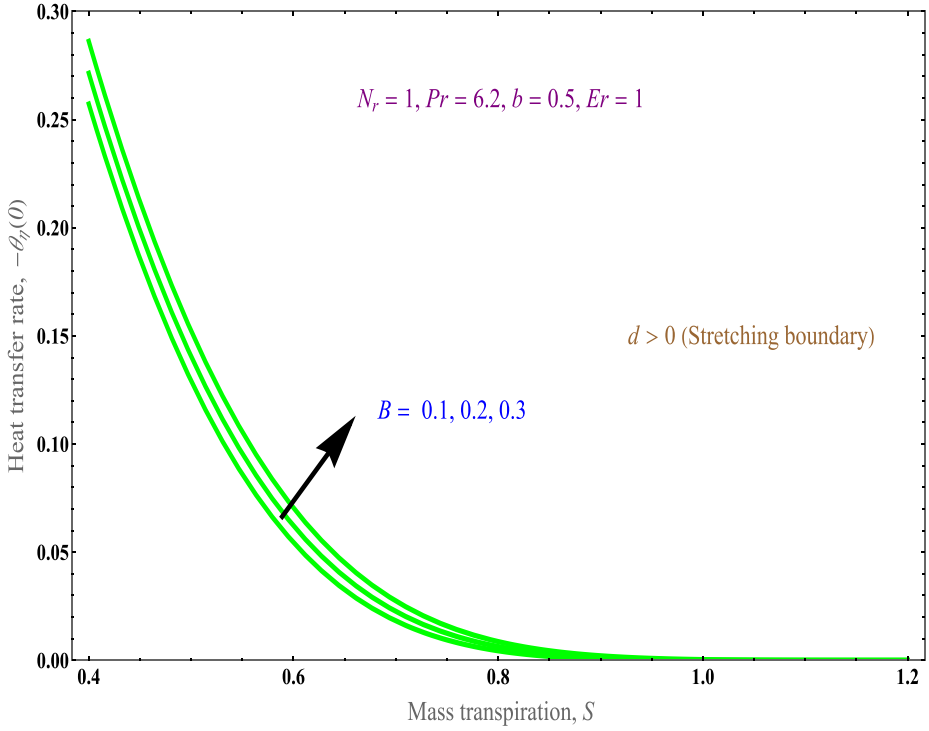

Fig. 22. Graph of heat transfer rate with variation of temperature slip.

Table 1

Properties	H_2O	Au
ρ(kg m^{-3})	997.1	19300
C_p(J kg K^{-1})	4179	129
k(W m K^{-1})	0.613	318

thermal radiation parameter shows increasing nature for both shrinking/stretching boundary for both higher and lower branch solution.

Fig. 16(a) and (b) represents the temperature jump graphs for temperature profile with similarity variable, while keeping heat source/sink, radiation, micropolar, mass transfer parameters constant. The temperature decreases with increasing the thermal jump parameter. The first graph shrinking boundary exhibits the dual solution shows the increasing the positive slip parameter b decreases the both higher branch and lower branch solution. In the second graph for stretching boundary exhibits the unique solution and while rising the slip parameter b the solution shows decreasing in nature, slip parameter b shows decreasing nature for both shrinking/stretching boundary for both higher and lower branch solution.

Fig. 17(a) and (b) represents the mass transfer graph for temperature profile with similarity variable, while keeping heat source/sink, radiation, Eringen number, velocity slip parameters constant, the first graph shrinking boundary exhibits the dual solution shows the increasing the mass transpiration increases the both higher branch and lower branch solution, in the second graph for stretching boundary exhibits the unique solution and while rising the mass transfer the solution shows increasing in nature, mass transfer shows increasing nature for both shrinking/stretching boundary for both higher and lower branch solution.

Fig. 18 represents the heat transfer rate profile with mass transfer for different Eringen number, while keeping heat source/sink, radiation, velocity slip parameters constant. Increasing values of Eringen parameter is connected with stronger rheological effects which tends to decays the velocity gradient, Meanwhile, the velocity is declining, which reasons to decline the dissipation of energy and therefore the thermal gradient decrease thermal layer has an increase behavior for both positive and negative values of mass transpiration, the thermal boundary layer rises when the Eringen number rises for stretching boundary.

Fig. 19 represents the heat source/sink graph for heat transfer rate profile with mass transfer, while keeping micropolar, radiation, Eringen number, velocity slip parameters constant. The thermal layer has a decreasing behavior for both positive and negative values of mass transpiration, the thermal boundary layer decays when the heat source/sink parameter rises for the stretching boundary.

Fig. 20, represents the volume fraction graph for heat transfer rate profile with mass transfer, while keeping Eringen number, radiation, Eringen, velocity slip parameters constant. The thermal boundary layer upsurges when volume fraction parameter upsurges and with an amplification of nanoparticle volume fraction and thus the rate of heat

Table 2

Parameters	Eringen number Er	Mass transpiration S	Darcy number Da^{-1}	Volume fraction φ	Thermal radiation Nr	Heat source/sink Ni	Velocity slip b
Skin friction $f_{\eta\eta}(0)$	Increases	–	–	–	–	–	–
Reduced couple stress coefficient $g_\eta(0)$	Increases	–	–	–	–	–	–
Velocity profile $f_\eta(\eta)$	Decreases	Decreases	Decreases	Decreases	–	–	Decreases
Angular velocity $g(\eta)$	Decreases	Decreases	Decreases	–	–	–	Decreases
Temperature $\theta(\eta)$	Increases	Increases	–	Increases	Increases	Increases	Decreases
Heat transfer rate $-\theta_\eta(0)$	Increases	–	–	Increases	Increases	Decreases	Increases

Table 3
Comparison of the present study and related works by other authors.

Related Works by other Authors	Fluids	Value of Momentum solution
[40]	Newtonian	$\alpha = 1$
[43]	Newtonian	$\alpha = \sqrt{1+M}$
[20]	non-Newtonian	$f(\eta) = f_w + \frac{\lambda}{\beta_a}(1 - e^{-\beta_a \eta})$, $3f_w\left(\frac{\rho_{hnf}}{\rho_f}\right) \pm \beta_a = \frac{\sqrt{9f_w^2\left(\frac{\rho_{hnf}}{\rho_f}\right)^2 + 12\lambda\left(\frac{\rho_{hnf}}{\rho_f}\right)\left(\frac{\mu_{hnf}}{\mu_f}\right) + M\left(\frac{\sigma_{hnf}}{\sigma_f}\right)}}{2\left(\frac{\rho_{hnf}}{\rho_f}\right)}$
[44]	Newtonian	$f(\eta) = s - \frac{1 - e^{-\lambda\eta}}{\lambda}$, $\lambda = \frac{s \pm \sqrt{-4 - 2K + s^2}}{2 + K}$.
[37]	non-Newtonian	$f(\eta) = s + a\frac{1 - e^{-C\eta}}{C + bC^2}$, $(2 + R)bC^3 + (2 + R - 2sb)C^2 - 2sC - 2 = 0$.
Present work	non-Newtonian	$f(\eta) = S + d\frac{1 - e^{-\beta\eta}}{(\beta + b\beta^2)}$, $(2A_1 b + \mathrm{Er}b)\beta^3 + (2A_1 + \mathrm{Er} - 2A_2 Sb)\beta^2 - \left(2A_2 S + \frac{2A_1 b}{\mathrm{Da}}\right)\beta - \left(2A_2 d + \frac{2A_1}{\mathrm{Da}}\right) = 0$.

transfer enhances with increase of volume fraction of nano particles. For the stretching boundary, thermal layer has an increasing behavior for both positive and negative values of mass transpiration.

Fig. 21, represents the radiation graph for heat transfer rate profile with mass transfer, while keeping micropolar, heat source/sink, Eringen number, and velocity slip parameters constant, thermal layer has an increase behavior for both positive and negative values of mass transpiration, the thermal boundary layer increases when the radiation parameter increases for the stretching boundary.

Fig. 22 represents the velocity slip graph for heat transfer rate profile with mass transfer, while keeping Eringen number, heat source/sink, micropolar, velocity slip parameters constant. The thermal boundary layer upsurges when the temperature slip parameter upsurges, thermal layer has an increase behavior for both positive and negative values of mass transpiration for the stretching boundary.

A summary of the results can be tabulated as in Table 2.

Setting the numerical value of the Prandtl number Pr is 6.2 for water, and the range of parameters taken as Eringen number $0 \leq \mathrm{Er} \leq 5$, Mass suction/injection $-4 \leq S \leq 5$, inverse Darcy number $0.5 \leq Da^{-1} \leq 4$, thermal radiation parameter $0.1 \leq \mathrm{Nr} \leq 4$, volume fraction $0.1 \leq \varphi \leq 0.3$, velocity slip $0.1 \leq b \leq 5$, heat source/sink $0 \leq \mathrm{Ni} \leq 4$, thermal jump $0 \leq B \leq 4$ using physical properties given in Table 1, the table below shows that varying several parameters effect on momentum and temperature of the fluid flow.

Comparing to other works, this particular work generalises the overall solutions to include both heat and mass transfer. The table below (Table 3) compares the present study and other related works make themselves a special case of the current work.

6. Conclusion of remarks

Through this present investigation, we closely examine the micropolar fluid with suspension of nanofluid across a porous stretching/shrinking sheet with heat source and sink along with inclusion of thermal radiation with velocity and temperature slip boundary condition. The application arises in our study of advanced fuel cell and the results all show different ways in which the performance of the fuel cell can be improved.

With this schematic an objective in mind, the fluid flow field is analysed by converting the similarity variables. The momentum and temperature equations are converted to relevant ordinary differential equations solvable by analytical procedures. We found closed analytical solution for the significant physical characteristics like heat source/sink, velocity, and temperature slip, Eringen parameter, radiations have been examined in the present work. The following points are observed by the present work

- Dual solutions exist for the flow system, and there exists critical points around its solutions.
- For normal velocity the inverse Darcy number parameter shows increasing nature for stretching and showing reverse nature for shrinking boundary,
- The heat source/sink parameter shows increasing nature for both shrinking/stretching boundary for first branch solution,
- Mass transfer shows increasing nature for both shrinking/stretching boundary for both higher and lower branch solution.
- Thermal radiation parameter shows increasing nature for both shrinking/stretching boundary for both upper and lower branch solution.
- For normal and angular velocity micropolar parameter shows decreasing nature for shrinking/stretching boundary for first branch solution,

Limiting example of the current study is included in many previous researches as follows:

- If absence of porous media radiation, heat source and sink and nanofluids, {our results} → {results of [20]},
- If solution domain, velocity and temperature slip is zero, and mass transpiration is zero {our results} → {results of [40]}.
- If absence of heat source and sink and nanofluids, porous media {our results} → {results of [37]},

All these results present viable mechanisms to improve the flow structure and hence performance of the fuel cell. The implementation of these solutions will be investigated in future endeavours. Further extensions of the current work can be implemented incorporating new physical mechanisms, such as buoyancy effect, activation energy, viscoelastic fluid, or non-Newtonian fluid rheology over various geometries, like stretching/shrinking sheet, rotating disk, cylinder, cone, wedge, convergent/divergent channel, divergent channel, Riga plate, microchannel. etc.

Declaration of competing interest

The authors declare that they have no known competing financial interests or personal relationships that could have appeared to influence the work reported in this paper.

References

[1] Eringen AC. Simple micro fluids. Int J Eng Sci 1964;2:205.
[2] Eringen AC. Linear theory of micropolar elasticity. Journal of Mathematics and Mechanics 1996;15:909–23.
[3] Mahin O, Kolsi L, Amani M, Estelle P. Recent advances in modeling and simulation of nanofluid flows-part1: fundamentals and theory. Phys Rep 2019;790:1–48.
[4] Anusha T, Mahabaleshwar US, Sheikhnejad Y. An MHD od nanofluid flow over a porous stretching/shrinking plate with mass transpiration and brinkman ratio. Transport Porous Media 2022;142:333–52.
[5] Kim S, Kim H, Ahn H. Effects of nano-fluid and surfaces with nano structure on the increase of CHF. Exp Therm Fluid Sci 2010;34:487–95.
[6] Khan WA, Pop I. Boundary-layer flow of a nanofluid past a stretching sheet. Int J Heat Mass Tran 2010;53:2477–83.
[7] Mahabaleshwar US, Bognar GV, Baleanu D, Vishalakshi AB. Two-dimensional nanofluid due to an accelerated plate with viscosity ratio. Int J Algorithm Comput Math 2022;8:111.
[8] Wang CY. Stagnation flow towards a shrinking sheet. Int J Non Lin Mech 2008;43:377–82.

[9] Wani I, Ishak A, Pop I. Unsteady flow, and heat transfer past a stretching/shrinking sheet in a hybrid nano fluid. Transfer 2019;136:288–97.
[10] Dash GC, Tripathy RS, Rashidi MM, Mishra SR. Numerical approach to boundary layer stagnation-point flow past a stretching/shrinking sheet. J Mol Liq 2016;221:860–6.
[11] Nagaraju KR, Mahabaleshwar US, Krimpeni AA, Sarris IE. Impact of Mass transpiration on unsteady boundary layer flow of impulsive porous stretching sheet. Mathematical Modelling of Engineering Problems 2019;6:1327–37.
[12] Sachhin SM, Mahabaleshwar US, Huang HN, Sunden B, Zeidan D. An influence of temperature jumps and Navier's slip-on hybrid nanofluid flow over a permeable stretching/shrinking sheet with heat transfer and inclined MHD. Nanotechnology 2023;35(11):115401.
[13] Shahsafi A, Roney P, Kats MA. Temperature-independent thermal radiation. Proc Natl Acad Sci USA 2019;116:26402–6.
[14] Khan M, Hashim, Hafeez A. A review on slip-flow and heat transfer performance of nanofluids from a permeable shrinking surface with thermal radiation. Dual solutions 2017;173:1–11.
[15] Nadeem S, Zaheer S, Fang T. Effects of thermal radiation on the boundary layers flow of a Jefferey fluid over an exponentially stretching surface. Numer Algorithm 2011;57:187–205.
[16] Kenno T, Takahashi K, Sakai A. Detection of thermal radiation sensing of heat flux and recovery of waste heat by the transverse thermos electric effect. J Electron Mater 2014;43:13–22.
[17] Kumar S, Kumar D, Mahabaleshwar US. A new adjustment of Laplace transform for fractional Bloch equation in NMR flow. Applications and Applied Mathematics 2022;9:74–106.
[18] Maranna T, Sachhin SM, Mahabaleshwar US, Hatami M. Impact of Navier's slip and MHD on laminar boundary layer flow with heat transfer for non-Newtonian nanofluid over a porous media. Science Reports 2023;13(1).
[19] Mohan A, Sugunamma V, Raman JV. Influence of non-linear radiation on MHD 3D Casson Fluid flow past a non-linearly stretchingsheet with Non-uniform Heat Source/sink. International Journal of Trend in Research and Development 2016;3(3):93–4.
[20] Khan U, Zaib A, Ishak A, Roy NC, Bakar SA, Yahla IS. Exact solutions for MHD axisymmetric hybrid nanofluid flow and heat transfer over a permeable non-linear radially shrinking/stretching surface with mutual impacts of thermal radiation. European Physics Journal of Special Topics 2022;231:1195–204.
[21] Priyanka A, Kumar P, Baleanu D. Radiative MHD hybrid-nanofluids flow over a permeable stretching surface with heat source/sink embedded in porous medium. Int J Numer Methods Heat Fluid Flow 2021;9:pp39–55.
[22] Elshehawey EF, Elsayed ME, Nasser SE. Effect of inclined magnetic field on magneto fluid flow through a porous medium between two inclined wavy porous plates. Appl Math Comput 2003;135:80–6.
[23] Jalili B, Sadeghi S, Jalili P, Ganji DD. Characteristic of ferrofluid flow over a stretching sheet with suction with injection. Case Stud Therm Eng 2019;14:100–12.
[24] Ali F, Khan I, Shafie S. A note on new exact solution for some unsteady flows of Brinkman-type fluids over a plane wall. Z Naturforsch 2012;67:683–97.
[25] Barik RN, Dash GC. Thermal radiation effect on an unsteady magnetohydrodynamic flow past inclined porous heated plate in the presence of chemical reaction and viscus dissipation. Appl Math Comput 2014;226:423–34.
[26] Ibrahim FS, Elaiw AM, Bakr AA. Effect of the chemical reaction and radiation absorption on the unsteady MHD free convection flow past a semi-infinite vertical permeable moving plate with heat source and suction. Commun Nonlinear Sci Numer Simul 2008;13:1056–66.
[27] Sneha KN, Mahabaleshwar US, Sheikhnejad Y. Heat and mass transfer of Walter's liquid b flow over a porous stretching/shrinking plate with mass transpiration and slip. Transport Porous Media 2020;142:383–405.
[28] Kasaeian A, Daneshazarian R, Mahian O, Kolsi L, Pop I. Nanofluid flow and heat transfer in porous media: a review of the latest developments. Int J Heat Mass Tran 2017;107:778–91.
[29] Broseta D, Medjahed F, Lecourtier J, Robin M. Polymer adsorption/retention in porous media: effects of core wettability on residual oil. SPE Advanced Technology 1995;3:103–12.
[30] Mishra NK, Muthukumar P, Panigrahy SA. A review on clean combustion within porous media. Air Pollution and Control 2018:209–24.
[31] Reddy VS, Kandasamy J, Sivanandam S. Impacts of Casson Model on Hybrid Nanofluid flow over a moving thin needle with Dufour and Soret and thermal radiation effects. Math Comput Appl 2022;28:2–15.
[32] Khan M, Alshomrani AS. Numerical simulation for flow and heat transfer to Carreu fluid with magnetic field effect: dual nature study. J Magn Magn Mater 2017;443:13–21.
[33] Khonsari MM, Brewe DE. On the performance of finite journal bearings lubricated with micropolar fluids. Tribol Trans 2008:155–60.
[34] Hadimoto T. Two-dimensional shear flows of linear micropolar fluids. Int J Eng Sci 1969:515–22.
[35] Lockwood FE, Benchaita MT, Friberg SE. Study of lyotropic liquid crystals in viscometric flow and elastohydrodynamic contact. ASLE Transactions 2008;30:539–48.
[36] Ariman T, Turk MA, Sylvester ND. Applications of microcontinuum fluid mechanics. Int J Eng Sci 1974;12:273–93.
[37] Usafzai WK, Aly EH. Multiple exact solutions for micropolar slip flow and heat transfer of a bidirectional moving plate. Therm Sci Eng Prog 2023;37:101584.
[38] Aman S, Ismail Z, Salleh MZ. Impacts of gold nano particles on MHD mixed convection Poiseuille flow of nanofluid passing through a porous medium in the presence of thermal radiation, thermal diffusion and chemical reaction. Neural Computers, and Applications 2018;30:789–97.
[39] Freidoonimehr N, Rahimi AB. Exact-solution of entropy generation for MHD nanofluid flow induced by a stretching/shrinking sheet with transpiration: dual solution. Adv Powder Technol 2017;28:671–85.
[40] Crane LJ. Flow past a stretching plate. Z Angew Math Phys 1970;21:645–7.
[41] Ahmadi G. Self-similar solution of Incompressible Micropolar boundary layer flow over a semi-infinite plate. Int J Eng Sci 1976;14:639–46.
[42] Jena SK, Mathur MN. Similarity solutions for laminar free convectional flow of a thermos micro polar fluid past a non-isothermal vertical flat plate. Int J Eng Sci 1981;19:1431–9.
[43] Pavlov KB. Magnetohydrodynamic flow of incompressible viscous fluid caused by of a surface. Magnitaya Gidrodinamika 1974;4:146–7.
[44] Turkyilmazoglu M. A note on micropolar fluid flow and heat transfer over a porous shrinking sheet. Int J Heat Mass Tran 2014;72:388–91.
[45] Shen T, Xie H, Gavurova B, Sangeeta M, Karthikeyan C, Praveenakumar TR, Xia C, Manigandan S. Experimental analysis of photovoltaic thermal system assisted with nanofluids for efficient electrical performance and hydrogen production through electrolysis. Int J Hydrogen Energy 2023;48(55):21029–37.
[46] Sahin F, Acar MC, Genc O. Experimental determination of NiFe2O4-water nanofluid thermophysical properties and evaluation of its potential as a coolant in polymer electrolyte membrane fuel cells. Int J Hydrogen Energy 2024;50:1572–83.
[47] Rathore N, Sandeep N. Solar thermal energy performance on mono/trihybrid nanofluid flow through the evacuated thermal collector tube. Int J Hydrogen Energy 2023;48(94):36883–99.
[48] Pedersen-Mjaanes H, Chan L, Mastorakos E. Hydrogen production from rich combustion in porous media. Int J Hydrogen Energy 2005;30(6):579–92.
[49] Zhou Y, Liu Y, Shi Y, Zhang Y, Li Z, Shi J. Numerical investigation of extracted position characteristics in porous media with lean methane and air premixtures combustion. Int J Hydrogen Energy 2023;48(67):26394–406.
[50] Huang Z, Shi Z, Wang H, Wei J, Li Y, Peng Q, Yan F, Tu Y. Orthogonal analysis of multi-factors of hydrogen-fueled combustion in a micro recuperative planar with porous media. Int J Hydrogen Energy 2024;49:208–21.
[51] Li S, Xu Z, Wang F, Xu Z, Liu Z, Li P, Li M. Flame propagation characteristics and thermal radiation hazards of methane-hydrogen-mixed cloud explosion in unconfined area: experiment research and theoretical modeling. Int J Hydrogen Energy 2024;54:1563–74.
[52] Kuroki T, Sakoda N, Shinzato K, Monde M, Takata Y. Temperature rise of hydrogen storage cylinders by thermal radiation from fire at hydrogen-gasoline hybrid refueling stations. Int J Hydrogen Energy 2018;43(5):2531–9.
[53] Ghadikolaei SS, Gholinia M. Terrific effect of H2 on 3D free convection MHD flow of C2H6O2H2O hybrid base fluid to dissolve Cu nanoparticles in a porous space considering the thermal radiation and nanoparticle shapes effects. Int J Hydrogen Energy 2019;44(31):17072–83.